To be Submitted to
International Journal of Rock Mechanics and Mining Sciences

Modeling the Mechanical Behavior of Unsaturated Expansive Soils Based on Bishop Principle of Effective Stress

G.I. Ofoegbu
San Antonio, Texas 78228
gofoegbu@att.net

B. Dasgupta, C. Manepally, S.A. Stothoff
Center for Nuclear Waste Regulatory Analyses
Southwest Research Institute
6220 Culebra Road
San Antonio, Texas 78228

R. Fedors
U.S. Nuclear Regulatory Commission
11555 Rockville Pike
Washington, DC

Abstract
Modeling the mechanical behavior of expansive clays is of interest in understanding the performance of nuclear waste disposal designs that include clay materials as buffers around waste containers, backfill for underground openings, seals between adjacent openings, or as host-rock constituents. The buffers, backfill, and seals will be unsaturated during construction and will re-saturate at varying rates after cessation of disposal operations. The mechanical behavior of the clay materials during re-wetting could affect the pressure on waste containers, other engineered components, or the host rock, and could influence fluid flow and radionuclide transport. The authors describe an approach to mechanical modeling of unsaturated soils using the moisture retention characteristic curve and the Bishop principle of effective stress to evaluate suction effects on stress. The approach incorporates swelling, thermal expansion, and soil hardening and stiffening due to suction or compaction; and uses stress-strain relationships based on elastoplasticity. Suction contributions to soil stress, strength, and stiffness are evaluated using the same moisture retention characteristic curve that is a standard input for hydrologic modeling. The model is illustrated through several numerical simulations: oedometer compression, free-swell, and confined-swell testing of a bentonite-sand mixture and a granular bentonite mix; and the mechanical behavior of a bentonite column heated at the base and subjected to water infiltration at the top. The calculated results for the bentonite column are used to explore thermal-hydrological effects on the mechanical behavior of the column. Calculated axial pressure at the top of the column is compared with measured axial pressure from laboratory testing of similar materials and conditions. The calculated pressure compares well with the measurement. However, the model prediction is highly dependent on the swelling/shrinkage behavior of bentonite, which could be a source of uncertainty in estimating potential pressure due to a bentonite buffer in a nuclear waste repository design.

Keywords: expansive clay, bentonite, unsaturated, suction, bishop principle, swelling pressure

List of Symbols

σ_{ij}	Effective stress tensor (i, j are tensor indices)
σ_{ij}^{T}	Total stress tensor
$\sigma_{ij}^{\mathrm{NET}}$	Net stress tensor
u_a	Pore air (or gas) pressure
u_l	Pore liquid (water) pressure
u_{eq}	Equivalent pore pressure
s	Suction
p_s	Suction pressure
p	Effective pressure
q	Distortional stress intensity (proportional to second invariant of deviatoric stress tensor)
S_{ij}	Deviatoric stress tensor
χ	Bishop parameter
δ_{ij}	Kronecker delta (i, j are tensor indices)
S_l	Liquid (water) saturation
S_e	Effective saturation
S_r	Residual saturation
a_{bs}	Parameter used to define χ versus S_e relationships
Δe_{ij}	Increment (Δ) of total strain tensor (e_{ij})
Δe_{kk}	Increment of volumetric strain
Δe_{ij}^{E}	Increment of elastic strain tensor
Δe_{ij}^{P}	Increment of plastic strain tensor
ε^{P}	Plastic volumetric strain
Δe_{ij}^{Th}	Tensor of strain increment due to thermal expansion
Δe_{ij}^{CW}	Tensor of strain increment due to swelling
$\Delta \sigma_{ij}^{EX}$	Tensor of externally defined contribution to stress increment
C_{ijkl}	Elastic stiffness tensor (i, j, k, l are tensor indices)
K	Bulk modulus
K_∞	Maximum bulk modulus (K approaches K_∞ asymptotically as s increases)
G	Shear modulus
λ	Lamé modulus (elastic parameter)
ν	Poisson's ratio
V_b	Bulk volume of soil skeleton (network of mineral solids and pores)
V_s	Volume of (mineral) solids in the soil skeleton
μ	Specific volume
μ_0	Specific volume at start of a state increment
r_v	Void ratio
κ_r	Recompression slope of bilinear soil compression characteristic curve
λ_s	Virgin compression slope of bilinear soil compression characteristic curve
P_c	Preconsolidation pressure
P_{c0}	Preconsolidation pressure for zero-strain state and saturated condition
P_{cs}	Suction contribution to P_c
w	Product μp
T_s	Tensile strength
T	Absolute temperature (K)
M	Slope of critical state line in p-q space

F_s	Yield function value
Λ	Scalar factor used to define plastic flow rule
A_{ij}	Tensor used to evaluate plastic flow
Q_{ij}	Tensor used to evaluate plastic flow
θ_l	Gravimetric moisture content (ratio of mass of water to mass of solids)
α_{CW}	Unit swelling potential (volumetric strain increment per unit moisture content change)
α_{Th}	Thermal expansivity (volumetric strain increment per unit temperature change)

1 Introduction

Several proposed designs for disposal of high-level radioactive waste within water-saturated geologic media involve using expansive clays as part of the engineered barrier. In such designs, expansive clay could be used in buffers around the waste containers, backfill material for underground openings, or seals between adjacent openings. For example, a proposed Swedish design for nuclear waste disposal in a granitic host rock includes bentonite buffer, backfill and seals [1]. Also, expansive clays may occur in an argillaceous host rock. For example, the Opalinus Clay considered as a possible host rock for a repository in Switzerland [2] and the Callovo-Oxfordian clay considered in France [3] contain expansive clays similar to bentonite. In the designs, the clay buffer, backfill, or seal is planned to be constructed unsaturated and is expected to saturate with time after repository closure. Expansive clays are desired in such designs because of their ability to swell as they saturate. The swelling may cause small openings or fissures to seal and, thus, reduce fluid flow to and transport away from waste containers and increase the effectiveness of backfills or seals. Also, depending on mechanical constraints around the buffer, backfill, or seal, pressure generated by clay swelling may apply additional loading to other components of the engineered barrier that may need to be resolved in order to evaluate the performance of such components. A mechanical constitutive model for unsaturated swelling soils is needed to evaluate potential swelling and swelling pressure for such engineered barrier designs.

The mechanical behavior of unsaturated soils differs from saturated soils because of the effects of suction. In this paper, the term “soil” is used to represent a “weak” natural aggregate of mineral grains that generally can be separated by gentle mechanical means such as agitation in water (e.g., [4], p. 3). Expansive soils are fine-grained and contain enough clay minerals that swell when wetted (i.e., expansive clays) such that the soil behavior on wetting and drying is dominated by the clay mineral behavior. This paper focusses on the mechanical behavior of bentonite-bearing soils, which comprise buffer or seal material in repository designs. Interactions between pore fluids (air and water) at the fluid interfaces in expansive and non-expansive soils result in suction, which increases the effective pressure that binds the soil particles. The increased effective pressure and resulting compaction of the soil skeleton can cause the soil strength and stiffness to increase. Therefore, unsaturated soils often exhibit greater stiffness, cohesion, and preconsolidation pressure relative to the equivalent saturated soil [5].

The principle of effective stress for unsaturated soils, proposed by Bishop [6], defines the suction contribution to the effective stress through a parameter χ (Bishop parameter) and can be described through the following relationship

$$\sigma_{ij} = \sigma_{ij}^{T} + (u_a - \chi s)\delta_{ij} \tag{1}$$

$$s = u_a - u_l \tag{2}$$

where tensile stress is considered positive; σ_{ij} is the effective stress; σ_{ij}^{T} is the stress due to external loads such as gravity or applied surface traction and is commonly referred to as “total” stress; s is suction (also referred to as capillary pressure); u_a is the air or gas pressure; u_l is liquid-water pressure; δ_{ij} is the Kronecker delta ($\delta_{ij} = 1$ if $i = j$ and $\delta_{ij} = 0$ if $i \neq j$); and indices such as i and j range from 1 to 3 and represent components along Cartesian coordinate directions (a repeated index represents a summation over the range of the index). Reference [7] suggested that χ depends mainly on the liquid saturation S_l but may be affected by soil structure

and the wetting, drying, or stress change path. Also, as [7] explained, Eq. (1) is subject to a restriction that $\chi = 1$ for fully saturated soils and $\chi = 0$ for dry soils, which makes the equation consistent with the Terzaghi principle of effective stress for water-saturated or dry soils. Indeed, associating the quantity in parenthesis in Eq. (1) with an equivalent pore-fluid pressure u_{eq} results in the following.

$$u_{eq} = u_a - \chi s = (1-\chi)u_a + \chi u_l; \quad p_s = -u_{eq} \tag{3}$$

Eq. (3) gives $u_{eq} = u_a$ if $\chi = 0$ (i.e., dry soil) and $u_{eq} = u_l$ if $\chi = 1$ (i.e., water-saturated soil). In general, $0 < \chi < 1$ for an unsaturated soil and u_{eq} is negative and contributes a compressive part to the effective stress through Eq. (1). The magnitude of the compressive contribution represents the effects of pore fluid interface interactions on soil stress and is referred to in this paper as the suction pressure, denoted p_s and defined in Eq. (3).

The use of the effective stress equation for saturated soil [i.e., Eq. (1) with $\chi = 1$] has been well accepted in soil engineering. However, the more general effective stress concept for variably saturated soils [i.e., Eq. (1) for $0 \leq \chi \leq 1$] has met with skepticism related to the more complicated and coupled mechanical and hydrological behavior of unsaturated soils. Reference [8] identified the concerns with Eq. (1) as follows.

The first concern is a philosophical argument that introducing the constitutive parameter χ into a stress state definition violates a requirement that equilibrium states be definable in terms of stresses and external loading alone and independent of constitutive behavior. The argument emphasizes that soil constitutive behavior is introduced to link the equilibrium definition to soil deformation but should not be introduced directly into the stress state definition. However, the equilibrium states of a soil are defined in terms of total stress, not the effective stress. The concept of effective stress was introduced to obtain a stress measure suitable for developing meaningful stress-strain relationships. Therefore, effective stress and the χ parameter are part of the constitutive definition of the stress-deformation response but have no effect on the equilibrium relationship between total stress and external loading. Therefore, defining the effective stress in terms of a constitutive parameter should not raise any concern regarding the equilibrium state definition.

The second concern is that Eq. (1) is not single-valued for the effective stress because of path dependence. Indeed, S_l-s relationships are path-dependent. Hysteresis in moisture retention curves has been described through laboratory and field data (e.g., [8]) and several constitutive relationships have been proposed for modeling such hysteresis [9]. Laboratory data in [10] indicate that hysteresis in the moisture retention curve appear more important for the FEBEX bentonite than for the MX-80 bentonite. Therefore, if χ is defined as a function of S_l as suggested in [7], then hysteretic S_l-s relationships imply that the value of χ for a given s is path-dependent. However, the path dependence does not in any way invalidate Eq. (1).

The third concern is that χ is difficult to evaluate. Evaluating χ directly through Eq. (1) is not possible because effective stress cannot be measured. Although χ can be evaluated indirectly through shear strength (e.g., [13]), a better approach is to evaluate it using the moisture retention curve by implementing the suggestion in reference [7] that χ could be described as a function of S_l. This approach is better because the development of moisture retention curves for unsaturated clay soils is well established in groundwater hydrology (e.g., [8]). Therefore, all that is needed to evaluate χ using this approach is to establish reliable χ-S_l relationships.

An approach to modeling the mechanical behavior of unsaturated soils that has gained considerable use is based on splitting the right-hand side of Eq. (1) into two parts that are considered independent enough to be treated as separate stress-state variables (e.g., [5, 8]). In the approach, the stress state in unsaturated soil is described in terms of two independent variables, net stress ($\sigma_{ij}^{\mathrm{NET}}$) and suction ($s$), where s is as defined in Eq. (2) and $\sigma_{ij}^{\mathrm{NET}}$ is defined as follows.

$$\sigma_{ij}^{\mathrm{NET}} = \sigma_{ij}^{T} + u_a \delta_{ij} \tag{4}$$

As explained in [5], constitutive modeling using this approach consists of developing separate models for the contributions of net stress and suction to soil strain and adding the contributions to obtain the overall stress-strain relationships. This approach avoids the use of an "effective stress," and, therefore, the evaluation of a "Bishop" parameter. However, the approach involves defining suction-versus-strain relationships, which may be difficult to evaluate.

Although the approach based on two independent stress-state variables has been studied extensively (e.g., [5, 14]), the authors chose to develop a constitutive model based on Eq. (1) for the following reasons. First, the evaluation of χ can be handled reasonably well by using the soil moisture characteristic curve (also referred to as the moisture retention curve), thereby addressing the third concern with the Bishop principle of effective stress. An approach to the evaluation is described in Section 2.1. Second, having defined the effective stress using Eq. (1), stress-strain relationships can be developed using standard elasto-plasticity theory without a need to define new concepts. Finally, the resulting constitutive model can be implemented in an existing geomechanics modeling code using a standard user interface for the code. This paper describes the development and evaluation of a mechanical constitutive model for unsaturated expansive soils based on this approach. The model, referred to hereafter as Modified Cam-clay model for Unsaturated Soil (MCUS), is described in Chapter 2 and has been numerically coded for implementation in FLAC [15]. Chapter 3 describes example numerical modeling conducted using the implementation.

2 Constitutive Model

The constitutive model defines relationships between increments of strain and effective stress in an unsaturated expansive clay soil subjected to wetting (or imbibition) and drying (or drainage) cycles, temperature change, and external loading. We describe the evaluation of Bishop parameter χ and suction pressure (i.e., suction contribution to the effective stress) p_s as functions of suction s; general incremental stress-strain relationships; and models for elastic deformability, plastic strain and yielding, and strains due to swelling or shrinkage and thermal expansion.

2.1 Evaluation of Bishop parameter and suction pressure

The evaluation of χ involves defining χ-S_l and S_l-s (moisture retention) relationships. Regarding the χ-S_l relationship, a common practice is to assume $\chi = S_l$ [16, 17, 18]. However, some published data (e.g., [8], p. 40) suggest that $\chi \leq S_l$ and $\chi \geq S_l$ can all be expected. Therefore, the authors propose the following to provide for a flexible range of χ-S_l relationships.

$$\chi = \frac{S_e}{a_{bs} + (1 - a_{bs}) S_e} \tag{5}$$

$$S_e = (S_l - S_r)/(1 - S_r) \quad (6)$$

where S_e is the effective saturation (e.g., [8], p. 112), defined in Eq. (6) using the residual saturation S_r but could be defined by replacing S_r with an immobile fraction of the liquid saturation such as suggested in [19]. The parameter a_{bs} could represent the effects of soil type; has to be positive; but can be less than, equal to, or greater than unity ($\chi = S_e$ if $a_{bs} = 1$). A graphical representation of Eq. (5) (Fig. 1) shows that the suction contribution to the effective stress through Eq. (1) decreases as a_{bs} increases, such that a value of a_{bs} greater than ~10 could make the role of suction insignificant in any case. Therefore, as the figure suggests, the value of a_{bs} should not exceed a maximum that could be material dependent in order to represent the effects of suction through Eq. (1).

Having defined a χ-S_l relationship using Eq. (5), evaluating χ and p_s requires a material-specific moisture retention relationship. The authors obtained hydrological and mechanical properties data for an MX80 bentonite and quartz sand mixture in dry weight proportions of 70% bentonite and 30% sand [20, 21] and for a granular MX80 bentonite specimen referred to as E-Mix [22]. The data were part of information provided for the **DE**velopment of **CO**upled Models and Their **VAL**idation against **EX**periments (DECOVALEX) program, an international program on modeling coupled thermal, hydrological, chemical, and mechanical processes relevant to the performance of designs for geologic disposal of nuclear waste [23]. The two sets of data are used here to illustrate the evaluation of χ and p_s.

2.1.1 Evaluation of χ and p_s for a bentonite-sand mixture

The information for the bentonite-sand mixture included moisture retention data obtained under constant volume conditions and provided in terms of moisture content (θ_l) versus s. However, the measured maximum θ_l was greater than the theoretical value for saturated conditions, which suggests that the specimen did swell somewhat during the test. Therefore, the authors corrected the θ_l values to remove the swelling effect and ensure S_l does not exceed 1.0. Also, the authors assumed $S_r = 0.15$ based on examination of the data. The resulting S_e-s data was fit with the following equation.

$$S_e = 1 - \frac{s}{a+bs} \quad (7)$$

with $a = 12.5$ and $b = 1.25$ for s in MPa. The measured data and fitted relationship are shown in Fig. 2. The χ-s relationship for the bentonite-sand mixture is obtained by substituting Eq. (7) into Eq. (5) and is shown in Fig. 3. The suction pressure p_s is obtained as χs (for $u_a = 0$) and shown in Fig. 4. As Figs. 3 and 4 show, χ decreases monotonically from a value of 1.0 at saturation and p_s increases monotonically from zero at saturation as s increases. The relationships depend strongly on a_{bs} and a value of a_{bs} of 10 or greater appears inappropriate for this material because of its effect on p_s. Because the moisture retention data does not include hysteresis, the χ-s and p_s-s relationships obtained using the data are non-hysteretic. However, a hysteretic moisture retention behavior can be incorporated using the same procedure described in this subsection.

2.1.2 Evaluation of χ and p_s for MX80 E-Mix granular bentonite

The authors fit the following S_e-s relationship to the moisture retention data for the MX-80 E Mix granular bentonite from reference [22].

$$S_e = \text{MIN}\left\{1.0, \left[0.6 + \frac{40-s}{a+c(40-s)}\right]\right\} \quad \text{for} \quad 0 \le s \le 40 \text{ MPa} \tag{8}$$

$$S_e = 0.6 - \frac{s-40}{a+b(s-40)} \quad \text{for} \quad s > 40 \text{ MPa} \tag{9}$$

where $a = 85$, $b = 1.75$, and $c = 0.05$ with s in MPa. The relationship is shown in Fig. 5 along with a van Genuchten [24] fit to the same data. Although the van Genuchten function is considered standard and used extensively by hydrologists, the authors chose Eqs. (8) and (9) to simplify subsequent use of the moisture retention data in mechanical constitutive modeling. The χ-s relationship for the granular bentonite is obtained by substituting Eqs. (8) and (9) into Eq. (5) and is shown in Fig. 6. The suction pressure p_s is obtained as χs (for $u_a = 0$) and shown in Fig. 7. As Fig. 7 shows, p_s increases monotonically with s for $a_{bs} \le 1.5$. Therefore, the authors consider values of a_{bs} greater than 1.5 as inappropriate for this material because there is no physical reason for a decrease in p_s as s increases, i.e., the slope $\partial p_s/\partial s$ should always be positive even if its magnitude decreases as s increases.

2.2 General stress-strain relationships for a heated expansive clay soil

Based on common practice in stress-strain modeling of elastic-plastic materials (e.g., [25]), the authors assume that the contributions to the strain increment at a point in the soil mass (i.e., over a representative elementary volume of the soil) are additive and separable. The relevant strain increments for a heated expansive clay soil are the elastic, Δe_{ij}^E; plastic, Δe_{ij}^P; thermal, Δe_{ij}^{Th}; and physicochemical swelling, Δe_{ij}^{CW}. The elastic and plastic strains represent recoverable and non-recoverable deformations due to mechanical loads; thermal strains are associated with thermal expansion; and physicochemical strains are associated with swelling due to water absorption (or shrinkage due to water loss) but do not include any deformation due to a release of mechanical loading, which is included in the elastic strain. The assumption that the strain increment contributions are additive implies that the total strain increment, Δe_{ij}, during a state change from time t to time $t + \Delta t$ is given by

$$\Delta e_{ij} = \Delta e_{ij}^E + \Delta e_{ij}^P + \Delta e_{ij}^{Th} + \Delta e_{ij}^{CW} \tag{10}$$

where tensile strain is considered positive. An important implication of Eq. (10) is the incremental stress-strain relations can be based on Hooke's law and results in the following

$$\Delta\sigma_{ij} = C_{ijkl}\left(\Delta e_{kl} - \Delta e_{kl}^P - \Delta e_{kl}^{Th} - \Delta e_{kl}^{CW}\right) \tag{11}$$

where C_{ijkl} is the elastic stiffness matrix and, assuming the material is isotropic with respect to mechanical deformation, can be evaluated using the following

$$C_{ijkl} = \lambda\delta_{ij}\delta_{kl} + G\left(\delta_{ik}\delta_{jl} + \delta_{il}\delta_{jk}\right) \tag{12}$$

with shear modulus G and Lame parameter λ related to the bulk modulus K and Poisson's ratio ν through the following

$$\lambda = \frac{3K\nu}{1+\nu} \quad \text{and} \quad G = \frac{3}{2}(K - \lambda) \tag{13}$$

Eq. (11) is nonlinear because of the effects of compaction and pressure (hence, suction) on bulk modulus. We implement Eq. (11) as follows using a FLAC® [15] "extra variable" interface.

$$\Delta\sigma_{ij} = C_{ijkl}\left(\Delta e_{kl} - \Delta e_{kl}^{P}\right) - \Delta\sigma_{ij}^{\mathrm{EX}};\quad \Delta\sigma_{ij}^{\mathrm{EX}} = C_{ijkl}\left(\Delta e_{kl}^{Th} + \Delta e_{kl}^{CW}\right) \tag{14}$$

34

where $\Delta\sigma_{ij}^{\mathrm{EX}}$ is treated as an externally defined addition to the stress increment and is not affected by Δe_{kl}^{P}. This implementation is based on two assumptions: (1) the effects of soil deformation on thermal-hydrological processes (that drive moisture redistribution and temperature change) can be neglected during a small increment of the mechanical state and (2) the bulk modulus K (therefore, components of C_{ijkl}) can be treated as constant during such increment and updated at the end of the increment.

2.3 Deformability and preconsolidation

We describe soil strain in terms of the specific volume history, where specific volume μ is the ratio of bulk volume V_b to volume of solids V_s and is related as follows to the void ratio r_v.

$$\mu = \frac{V_b}{V_s} = 1 + r_v \tag{15}$$

If the compressibility of solid particles is assumed negligible such that $\Delta V_s/V_s \approx 0$, it can be shown that the specific volume is related as follows to the volumetric strain increment (where μ_0 is the specific volume at the start of the increment).

$$\mu = \mu_0(1 + \Delta e_{kk}) \tag{16}$$

An increase in μ indicates dilation and a decrease indicates compaction. The change may be recoverable (i.e., elastic) or non-recoverable (i.e., plastic) as discussed subsequently.

2.3.1 Specific volume versus pressure

The volume change versus pressure model is based on the laboratory soil compression characteristic curve described schematically in Fig. 8. As the figure shows, the characteristic curve is represented by a bilinear μ- $\log p$ relationship OAB, where p represents pressure. The OA segment with a slope κ_r represents the unloading-reloading response and the AB segment with a slope λ_s represents the virgin compression response. The pressure at which virgin compression begins, i.e., the break in the bilinear relationship (point A in Fig. 8), is approximately equal to the preconsolidation pressure (P_c), which represents the maximum effective pressure that the soil element experienced previously (e.g., [4], p. 103). The soil is described as "over-consolidated" if $p < P_c$ or "normally consolidated" if $p = P_c$. Volume change response under over-consolidated conditions is purely elastic whereas both elastic and plastic deformations may occur under normally consolidated conditions. For a normally consolidated soil, P_c increases as μ decreases (i.e., soil compaction). Also, an increase in suction (i.e., soil drainage or drying) causes P_c to increase. The effects of compaction and suction on P_c are described in more detail as part of the plasticity model.

Because the soil compression characteristic curve is described with respect to a $\log p$ scale, an arbitrary minimum pressure p_{ref}, referred to as reference pressure, needs to be included with the material specification. The compression behavior is undefined in the model for $p < p_{\mathrm{ref}}$,

except as modified in the plasticity implementation to account for a limited tensile strength. The value of specific volume at p_{ref}, referred to as the reference specific volume μ_{ref0}, is needed as part of the material specification and generally decreases as suction increases. The relationship between specific volume and pressure is based on the characteristic curve and is defined as follows.

$$\Delta\mu = -\kappa_r \frac{\Delta p}{p} \quad \text{for } p \le P_c \text{ (unloading or reloading)} \tag{17}$$

$$\Delta\mu = -\lambda_s \frac{\Delta p}{p} = -\lambda_s \frac{\Delta P_c}{P_c} \quad \text{for } p = P_c \text{ (virgin compression)} \tag{18}$$

The parameters P_c, κ_r, λ_s, and μ_{ref0} vary with suction as described in Section 2.5.

2.3.2 Elastic deformability

The elastic deformability is defined by the stress-strain relationships for over-consolidated (i.e., unloading-reloading) conditions. It can be shown using Eqs. (16) and (17) that the bulk modulus K is related to μ and p as follows.

$$K = \frac{\mu p}{\kappa_r} \tag{19}$$

Thus the elastic deformation is nonlinear, because the bulk modulus varies with deformation and pressure. Also, K is suction dependent, mainly because of suction pressure (e.g., Figs. 4 and 7) but also because of the effect of suction on μ through deformations caused by suction-dependent stress change.

For conditions of high suction, Eq. (19) could result in K values large enough to cause numerical instability. Therefore, the authors propose the following relationship to limit the value of K.

$$K = \frac{1}{\kappa_r}\left[w_0 + \frac{w - w_0}{1 + b_k(w - w_0)}\right] \tag{20}$$

$$b_k = \frac{1}{\kappa_r K_\infty - w_0} \tag{21}$$

where $w = \mu p$ and $w_0 = \mu_0 p_0$ is the value of w at the preconsolidation state under zero-strain and saturated conditions. The value of w_0 is determined by μ_{ref0}, κ_r, and P_{c0} (zero-strain value of P_c for a saturated condition) and the condition $w = w_0$ defines a minimum K. An alternative minimum K could be defined by evaluating w_0 at the reference state for saturated conditions (i.e., with $\mu_0 = \mu_{\text{ref0}}$ for saturated condition and $p_0 = p_{\text{ref}}$). The value of K from Eq. (20) approaches K_∞ asymptotically as s increases. However, the choice of K_∞ is somewhat subjective but can be controlled because a value that is too large may cause numerical problems whereas a value that is too small will likely result in a calculated unloading-reloading behavior that is incompatible with the measured behavior from an oedometer compression test. Choosing K_∞ is discussed with examples in Chapter 3 of this paper.

Fig. 9 shows K-s relationships based on Eq. (20) for the MX80 E-Mix granular bentonite (Section 2.1.2). Three relationships are shown in the figure for $K_\infty = 50$ MPa with w_0 evaluated at the preconsolidation state, $K_\infty = 100$ MPa with w_0 evaluated at the preconsolidation state, and $K_\infty = 100$ MPa with w_0 evaluated at the reference state. In each case w_0 is evaluated using

parameters for saturated condition. Evaluating w_0 at the preconsolidation state is based on an assumption that the preconsolidation state under saturated condition defines a minimum stiffness in the same way that it defines a minimum shear strength. The alternative reasoning, which results in evaluating w_0 at the reference state, is that while the effect of preconsolidation compaction may be preserved, the stiffness may still decrease because of pressure decreasing. The authors have not made a firm choice between the two options but intend to evaluate both to examine their effects for different modeling situations.

An additional parameter such as G or ν is needed in Eq. (13) to complete the elastic deformability model for a mechanically isotropic material. The authors have held ν constant, thereby letting G vary according to Eqs. (13) and (20). A conceivably better option that the authors have not evaluated is specifying ν as a function of s with a maximum value at $s = 0$ and an asymptotic minimum as s increases to large values. Such a relationship appears consistent with the effect of suction on soil stiffness but appears to be a model refinement relative to the model based on the constant ν assumption.

2.3.3 Inelastic deformation

Both elastic (recoverable) and inelastic (non-recoverable) straining may occur in a soil element undergoing deformation under normally consolidated conditions. Therefore, the virgin compression slope λ_s includes contributions due to elastic and inelastic deformations. Thus, soil deformability in a normally consolidated state is determined by the elastic deformability and the effects of inelastic deformation. We evaluate the contribution of inelastic deformation based on a generalized plasticity model as described in Section 2.4.

2.4 Generalized plasticity model

The plasticity model is based on defining the conditions for plastic deformation, referred to as the yield criterion; the rates (or incremental magnitudes) of plastic deformation using a flow rule; and the evolution of mechanical properties during plastic deformation, referred to as the hardening rule (cf. [26], p. 388).

2.4.1 Yield criterion

The yield criterion is based on modifying the CAM-Clay model yield function for saturated clay soils (e.g., [25]) to account for the effects of suction on yield strength. The CAM-Clay model provides a generalized representation of the volumetric and shearing behavior of soils, has been used extensively to model plastic yielding under saturated conditions, and has been shown to be well suited for unsaturated conditions if the effects of suction are incorporated appropriately (e.g., [5]). Consistent with the CAM-Clay model, the yield condition is defined in terms of an elliptical surface in p-q space, where p is the effective pressure and q is the distortional stress intensity (proportional to the second invariant of deviatoric stress, S_{ij}), defined as follows.

$$p = -\frac{1}{3}\sigma_{kk} \tag{22}$$

$$q = \sqrt{\frac{3}{2}S_{ij}S_{ij}} \tag{23}$$

$$S_{ij} = \sigma_{ij} - \frac{1}{3}\delta_{ij}\sigma_{kk} \tag{24}$$

As shown in Fig. 10, the major axis of the ellipse lies on the p axis and has a magnitude of $P_c + T_s$, where T_s is the tensile strength. The minor axis of the ellipse is parallel to the q axis and has a magnitude of $(M/2)(P_c + T_s)$, where M is the slope of the critical state line. The yield function, derived using the geometry of the yield surface, is as follows.

$$F_s = q^2 + M^2[p^2 + (T_s - P_c)p] + (M^2/4)[(T_s - P_c)^2 - (T_s + P_c)^2] = 0 \tag{25}$$

The condition $F_s < 0$ represents stress states within the interior of the yield surface and defines over-consolidated conditions, i.e., stress conditions that permit only elastic deformation. The condition $F_s = 0$ represents stress states on the yield surface and defines normally consolidated conditions, i.e., stress conditions that permit elastic and inelastic (i.e., plastic) deformations. The condition $F_s > 0$ is not permissible and represents a stress state estimate that must be corrected back to the yield surface to obtain a stress state valid for describing the elastic-plastic conditions. The yield surface may expand if P_c increases (e.g., due to compaction) or shrink if P_c decreases. The dependence of the yield surface on compaction implies a dependence on the plastic volumetric strain (ε^P), as indicated in Fig. 10. The location of the yield function in p-q space as Fig. 10 shows is based on q being positive or zero while p varies in $-T_s \leq p \leq P_c$.

2.4.2 Plastic strain increment using plastic flow rule

The flow rule is based on a potential function H in the effective stress space such that the plastic strain increment is proportional to the gradient of H with respect to stress as follows.

$$\Delta e_{ij}^P = \Lambda \frac{\partial H}{\partial \sigma_{ij}} \tag{26}$$

where Λ is a positive scalar variable. The CAM-Clay model was developed to ensure that a plastic potential identical to the yield function (i.e., $H \equiv F_s$) provides a compaction and dilation behavior consistent with the observed behavior of clay soils. Such a plastic potential is said to be “associated” with the yield function. Therefore, Eq. (26) with $H \equiv F_s$ results in an associated flow rule, which implies that the plastic strain increment vector at any point on the yield surface coincides with the outward normal to the yield surface. Therefore, as indicated in Fig. 10, plastic deformation at stress states on the right-hand side of the minor axis of the ellipse (dashed line in Fig. 10) results in compaction. Conversely, plastic deformation at stress states on the left-hand side of the minor axis results in dilation. Plastic deformation at a stress state represented by the intersection of the minor axis with the yield surface (i.e., the so-called critical state) results in constant-volume shearing.

The following derivatives of the yield function and combinations of the derivatives with the elastic stiffness matrix are needed to evaluate the plastic strain increments using Eq. (26).

$$A_{ij} = \frac{\partial F_s}{\partial \sigma_{ij}} = 3S_{ij} - \frac{M^2}{3}(2p + T_s - P_c)\delta_{ij} \tag{27}$$

$$Q_{ij} = C_{ijkl}A_{kl} = 6GS_{ij} - \frac{M^2}{3}(2G + 3\lambda)(2p + T_s - P_c)\delta_{ij} \tag{28}$$

To evaluate Λ (therefore, Δe_{ij}^{P}), we invoke the consistency condition, which requires $\Delta F = 0$ for two successive stress states that permit plastic deformation (e.g., [26], p. 388). The consistency condition for Eq. (25) results in the following relationship that needs to be evaluated to enforce the condition.

$$\Delta F = \frac{\partial F_s}{\partial \sigma_{ij}} \Delta \sigma_{ij} + \frac{\partial F_s}{\partial P_c} \Delta P_c = 0 \tag{29}$$

The following expression is obtained for Λ by substituting Eqs. (14) and (25)–(28) into (29).

$$\Lambda = \frac{1}{Q_D} Q_{ij} \Delta e_{ij} \tag{30}$$

$$Q_D = A_{ij} Q_{ij} + \left(\frac{\partial F_s}{\partial P_c}\right)\left(\frac{\mu P_c}{\lambda_s - \kappa_r}\right) A_{kk}; \quad \frac{\partial F_s}{\partial P_c} = -M^2 (p + T_s) \tag{31}$$

The evaluation of ΔP_c, which was used in the derivation of Eq. (31), is explained in the next subsection. Eqs. (26) and (30) are used in Eq. (14) to evaluate stress increments.

2.4.3 Evolution of the yield surface due to plastic deformation

Soil compaction, i.e., plastic deformation resulting in a permanent decrease in volume, causes an increase in P_c, which causes the yield surface to increase. Consider a deformation sequence under virgin compression conditions, i.e., stress state on the yield surface (on the ellipse in Fig. 10 or on AB in Fig. 8) during which the specific volume and preconsolidation pressure change from (μ, P_c) to $(\mu + \Delta\mu, P_c + \Delta P_c)$. The specific volume increment consists of an elastic part $\Delta\mu^E$ related to P_c and ΔP_c through Eq. (17) and a plastic part $\Delta\mu^P$. It can be shown using Eqs. (17) and (18) that

$$\Delta\mu^P = -(\lambda_s - \kappa_r)\frac{\Delta P_c}{P_c} \tag{32}$$

If the values of specific volume and preconsolidation pressure at the start of the deformation sequence are denoted ${}^0\mu$ and ${}^0P_c$, then it can be shown using Eqs. (16) and (32) that

$$\Delta P_c = -\left(\frac{{}^0\mu\ {}^0P_c}{\lambda_s - \kappa_r}\right)\left(\Delta e_{kk}^{P}\right) \tag{33}$$

$$P_c = {}^0P_c + \Delta P_c \tag{34}$$

Soil dilation due to plastic deformation on the left-hand side of the critical state (Fig. 10) will cause a decrease in P_c, because Δe_{kk}^{P} will be positive in such a case, which will result in a negative ΔP_c because the first parenthesis quantity in Eq. (33) is positive if values of λ_s and κ_r are appropriate.

2.5 Effects of suction on deformability and preconsolidation

The preconsolidation pressure P_c and deformability parameters κ_r, λ_s, and μ_{ref0} are suction dependent. The tensile strength T_s (therefore cohesion parameter c_s) and critical state line slope M (Fig. 10) likely are also suction dependent. We describe the suction dependency in this section based on available but at times unconfirmed information.

2.5.1 Preconsolidation pressure

The value of P_c at the initial state (i.e., state of zero deformation characterized by an initial pressure and initial void ratio), $P_{c\text{init}}$, consists of two parts as follows.

$$P_{c\text{init}} = P_{c0} + P_{cs} \tag{35}$$

where P_{c0} is the value for a saturated condition and P_{cs} is the suction contribution. $P_{c\text{init}}$ is suction dependent because of P_{cs}. For example, the suction dependency of P_{cs} for the granular bentonite mix described in Section 2.1.2 is illustrated in Fig. 11. As the figure shows, P_{cs} depends on the magnitude and history of s. For a soil element subjected to increasing s (i.e., drainage or drying phase), $P_{cs} = p_s$ and depends on a_{bs} as described in Fig. 7. The P_{cs}-s relationship for the granular bentonite mix in a drying phase is represented by the red curve in Fig. 11, which is the same as the $a_{bs} = 1$ curve in Fig. 7. During a wetting (or imbibition) phase, P_{cs} remains constant at the historical maximum as s decreases (e.g., horizontal green line in Fig. 11). When s is smaller than the air-entry value s_{aEp}, P_{cs} decreases with s as represented by the near vertical segment of the green bilinear relationship. Although described here as bilinear, the P_{cs}-s relationship during wetting is likely a curve parallel to the drainage (red) curve. During a re-drainage or re-drying phase beginning at a value of P_{cs} above the red curve, the P_{cs}-s relation would follow a curve parallel to and above the red curve but represented here by the blue dashed line, until the value of P_{cs} reaches the historical maximum.

At the initial state, $P_c = P_{c\text{init}}$ as defined using Eq. (35). Subsequently, for an incremental change in suction,

$$P_c = {}^0P_c + \Delta P_{cs}; \quad \Delta P_{cs} = \frac{\partial P_{cs}}{\partial s}\Delta s \tag{36}$$

where ${}^0P_c$ is the value of P_c at the previous resolved state. Eq. (36) is evaluated at the beginning of a deformation increment before the stress-strain calculations described in Sections 2.3 and 2.4. In contrast, Eqs. (33) and (34) are evaluated at the end of the increment. That is, the effects of suction on P_c are evaluated once at the beginning of a deformation increment, whereas the effects of compaction are evaluated once at the end of the increment.

2.5.2 Soil compression characteristic curve

The soil compression characteristic curves for the MX80 bentonite-sand mixture (Section 2.1) are shown in Fig. 12 based on reference [21] data. The data are based on laboratory oedometer compression tests at constant suction for four different suction values. The data can be used directly to evaluate P_{c0} (using the measured characteristic curve from the $s = 0$ test) and the μ_{ref0}-s relationship. Based on the data, we obtained $P_{c0} = 0.8$ MPa and the μ_{ref0}-s relationship shown in Fig. 13. The data indicates that μ_{ref0} decreases, and the gradient $\partial\,\mu_{\text{ref0}}\,/\partial s$ decreases asymptotically toward zero, as s increases. We fit a bilinear μ_{ref0}-s relationship to the data but a continuous curve may have worked at least as well as the bilinear relationship.

Fig. 12 data also could be used directly to evaluate κ_r and λ_s based on Eqs. (17) and (18). However, values of κ_r and λ_s calculated using this approach vary with pressure in a way that could result in excessive complication if the variation is incorporated in the constitutive model. Instead, we treated κ_r and λ_s as independent of pressure or deformation in Eqs. (17) and (18)

and performed numerically simulated oedometer compression testing (described in Chapter 3) to evaluate the parameters. The values of κ_r and λ_s calculated based on the simulated testing and fitted κ_r-s and λ_s-s relationships are shown in Fig. 14. The results suggest that κ_r decreases and λ_s increases, both asymptotically, as s increases.

2.6 Swelling and shrinkage

In this paper, physicochemical swelling or shrinkage refers to the strain contribution due to an increase or decrease of moisture content. Such swelling or shrinkage results from the increase or decrease of water that is sorbed within the platy structure of the clay minerals, in contrast to water held in place by interfacial tension at the soil-gas-liquid interface. The strain increment Δe_{ij}^{CW} in Eqs. (10), (11), and (14) is equal to one third of the potential volumetric strain increment due to an increase in moisture content for an elemental volume that is free to expand or shrink in every direction as the moisture content increases or decreases. This strain increment actually is fictitious as it is meaningful only for an isolated soil element subjected to a uniform moisture content change. The physicochemical strain increment in a real soil element connected to other elements and to a boundary surface consists of two parts. The first part represents potential free swelling or shrinkage if the element were isolated and is equal to Δe_{ij}^{CW}. The second part arises from interactions due to moisture-content and mechanical-property gradients within the soil medium and any boundary restraint. This second part is not represented explicitly but results from satisfying the equilibrium conditions and constitutive relationships for the medium. Swelling pressure occurs if part of the potential free swelling is suppressed due to moisture-content or mechanical-property gradients or boundary restraint.

The potential swelling of expansive clays is typically characterized using indices such as swelling potential, which is the percentage swelling measured in a “free-swell” test [8] or swelling pressure, which is the maximum pressure measured in a constant volume swell test [27]. These indices are useful for comparing different expansive clays or developing empirical design parameters, similar to approaches used in other geotechnical problems, such as the estimation of foundation heave [8]. However, for general mechanical modeling, including the evaluation of swelling pressure for a nuclear waste disposal design involving a bentonite clay buffer or seal, swelling is better characterized by defining the potential free swelling in relation to the moisture content change. We use a swelling characterization defined in terms of the potential free swelling strain per unit moisture content increment [28, 29], referred to here as the unit swelling potential α_{CW} and defined through the following equation.

$$\Delta e_{ij}^{CW} = (1/3)\alpha_{CW}(\Delta\theta_l)\delta_{ij} \tag{37}$$

where $\Delta\theta_l$ is the moisture content change. The coefficient α_{CW} can be evaluated as the gradient of the volumetric strain versus moisture content plot from an oedometer free-swell test.

2.6.1 Unit swelling potential for bentonite-sand mixture

Fig. 15 shows the volumetric strain versus moisture content based on oedometer free-swell test results from reference [21] and a curve fit used to approximate the data. The data indicate $\alpha_{CW} = 0$ for $\theta_l < 0.129$ and $\alpha_{CW} = 1.34$ for $\theta_l \geq 0.129$ for the bentonite-sand mixture. This interpretation of the data is based on an assumption that the total strain measured in the oedometer free-swell test is due to physicochemical swelling only. However, as discussed in reference [29], the measured volumetric strain from the oedometer free-swell test is the net effect of deformations due to suction reduction and swelling. Mechanical response to suction

reduction (i.e., deformations due to decrease in confining stress and bulk modulus) combine with the effects of swelling and could result in a measured volumetric strain that underestimates the swelling potential. However, a sensitivity analysis in reference [29] concludes that the value of α_{CW} based on the oedometer free-swell test provides a good estimate of the swelling behavior of the bentonite-sand mixture.

2.6.2 Unit swelling potential for MX80 E-Mix granular bentonite

The authors combined swelling strain versus time and moisture content versus time data based on oedometer free-swell test results in reference [22] to obtain swelling strain versus moisture content relationships for the MX80 E-Mix granular bentonite (Fig. 15). The data indicate a negligible dependence on the initial dry density, $\alpha_{CW} = 0$ for $\theta_l < \sim 0.073$, $\alpha_{CW} = 2.015$ for $0.073 \leq \theta_l \leq 0.878$, and $\alpha_{CW} = 1.16$ for $\theta_l > 0.878$.

2.6.3 Shrinkage

The authors have assumed that the unit shrinkage potential (i.e., value of α_{CW} for $\partial\, \theta_l / \partial t < 0$) and unit swelling potential (i.e., value of α_{CW} for $\partial\, \theta_l / \partial t > 0$) are equal and that the swelling threshold (i.e., smallest value of θ_l needed for swelling to initiate) is equal to the shrinkage limit. These assumptions imply full reversibility of swelling and shrinkage strains during wetting and drying cycles if the moisture retention curve is non-hysteretic. However, even with these assumptions regarding α_{CW}, a hysteretic moisture retention curve could result in the accumulation of non-reversible swelling or shrinkage strains during wetting and drying cycles. For example, reference [30] describes test results that indicate a net accumulation of swelling strain during cyclic wetting and drying of a densely compacted bentonite-silt mixture (initial dry density of 1.55 Mg/m^3) and net accumulation of shrinkage strain during cyclic wetting and drying of a loosely compacted specimen of the same soil (initial dry density of 1.27 Mg/m^3). In both cases the accumulated strain per cycle decreased as the number of cycles increased, such that the soil approached a state of full reversibility of swelling and shrinkage during wetting and drying cycles. However, the data did not indicate whether the observed strain accumulations are due to hysteretic swelling and shrinkage or hysteretic moisture retention.

Exposure of expansive soil to several wetting and drying cycles likely will not be of concern in potential designs for disposal of high-level radioactive waste in saturated geologic media. Expansive soils that are part of such a design will likely undergo one episode of re-wetting toward the ambient saturated condition, or one episode of increased drying followed by one episode of re-wetting toward the ambient condition. Potential uncertainty due to strain accumulation during such a drying and wetting history is likely smaller than the uncertainty that could result from several wetting and drying cycles.

2.7 Thermal expansion

The strain due to thermal expansion [i.e., Δe_{ij}^{Th} in Eqs. (10), (11), and (14)] is equal to one third of the potential volumetric strain increment due to a temperature increment ΔT for an elemental volume that is free to expand or contract in every direction as the temperature increases or decreases. As explained in Section 2.6 for physico-chemical swelling strain, this strain increment actually is fictitious as it is meaningful only for an isolated soil element subjected to a uniform temperature change. The thermal strain increment in a real soil element connected to other elements and to a boundary surface consists of two parts. The first part represents potential free thermal expansion or contraction if the element were isolated and is equal to Δe_{ij}^{Th}.

The second part arises from interactions due to temperature and mechanical-property gradients within the soil medium and any boundary restraint. This second part is not represented explicitly but results from satisfying the equilibrium conditions and constitutive relationships for the medium. A thermal stress increment occurs if part of the potential free thermal expansion is suppressed due to temperature or mechanical-property gradients or boundary restraint.

The thermal strain increment is related to the temperature change through the thermal expansivity, α_{Th}, as follows.

$$\Delta e_{ij}^{Th} = (1/3)\alpha_{Th}(\Delta T)\delta_{ij} \tag{38}$$

3 Example Modeling Cases

In this chapter we describe examples of numerical modeling conducted using the FLAC [15] implementation of MCUS. The examples consist of numerically simulated oedometer compression, oedometer free-swell and confined-swell tests, and mechanical behavior of a granular bentonite column heated at the base and subjected to water infiltration from the top.

3.1 Simulated oedometer compression testing

The simulated oedometer testing was conducted to determine κ_r-s and λ_s-s relationships [Eqs. (17) and (18)] needed to match the available laboratory data as discussed previously in Section 2.5.2. The geometrical model for the tests consists of a single axisymmetric rectangle with boundary-normal displacements held at zero at the base and side, and a downward displacement was applied at the top surface in small increments. The model was subjected to a uniform constant suction during each test. The suction values were chosen to match the available laboratory data and to cover the expected range of suction for the intended use of the simulated test results. The tests were performed for the bentonite-sand mixture and granular bentonite mix described previously in Sections 2.1.1 and 2.1.2.

3.1.1 Simulated oedometer testing of bentonite-sand mixture

For this material, we performed simulations for constant suction values of 0, 4.2, 12.6, and 38 MPa, which match the suction values for the laboratory compression tests from reference [21]. We set $a_{bs} = 1$ [Eq. (5)], $K_\infty = 1000$ MPa [Eq. (21)], $P_{c0} = 0.8$ MPa as discussed in Section 2.5.2, P_{cs} assigned from the $a_{bs} = 1$ curve in Fig. 4, and μ_{ref0} assigned from Fig. 13 as described in Sections 2.3.1 and 2.5.2. Then we determined through trial and correction the values of κ_r and λ_s needed to match the laboratory soil compression characteristic curve for each suction value. The resulting κ_r and λ_s values are given in Table 1 and Fig. 14. The calculated and laboratory compression curves are shown in Fig. 16 for the case of $s = 12.6$ MPa. The figure shows plots of μ versus p^T, where $p^T = p - p_s$ is the applied pressure, p is the effective pressure [Eq. (22)], and p_s is the suction pressure [Eq. (3)]. The unloading response for the $s = 0$ simulation case was numerically unstable for $p^T < \sim 2$ MPa.

The values of κ_r and λ_s in the numerical simulation were constrained by matching the laboratory data. An additional control, illustrated in Fig. 17, is that the value of p for a given μ on the virgin compression curve should increase monotonically as s increases. For a μ on the virgin compression curve, $p = P_{c\mathrm{init}} + \Delta p$ where Δp is related to $\Delta\mu$ through Eq. (18) and $P_{c\mathrm{init}}$ is defined in Eq. (35). Therefore, p is dominated by P_{cs}, which, as shown in Fig. 11 (red curve), increases monotonically with s. As Fig. 17 shows, the calculated results satisfy the additional

control, except for the simulation case for $s = 4.2$ MPa. We honored the laboratory data for this case. However, a different set of κ_r, λ_s, and μ_{ref0} values would have resulted in calculated results closer to the dashed lines in Fig. 17, to satisfy the additional control on $p(\mu)$ versus s.

3.1.2 Simulated oedometer testing of MX80 E-Mix granular bentonite

For this material, we performed simulations for $s = 0$, 10, 60, and 200 MPa to cover an expected range of suction for a different modeling task, but laboratory data was available for $s = 0$ only, from reference [22]. We set $a_{bs} = 1$, $K_\infty = 1000$ MPa, $P_{c0} = 2$ MPa from the $s = 0$ test data, and P_{cs} from the $a_{bs} = 1$ curve in Fig. 7. Then we determined the following through trial and correction with the additional control that the value of p for a given μ on the virgin compression curve should increase monotonically with s. For suction and pressure in MPa,

$$\mu_{\mathrm{ref0}} = 2.0 - \frac{s}{175+3.7s} \tag{39}$$

$$\kappa_r = 0.05 - \frac{s}{5000+25s} \tag{40}$$

$$\lambda_s = 0.23 + \frac{s}{100+20s} \tag{41}$$

The calculated soil compression curves and the laboratory data for $s = 0$ condition are shown in Fig. 18. The calculated results are also shown in Fig. 19 in terms of $p(\mu)$ versus s plots.

3.2 Simulated free-swell and confined-swell testing of bentonite-sand mixture

In the simulated swelling tests, a disk-shaped specimen, 2 m in diameter and 1 m thick, was modeled as an axisymmetric solid with boundary-normal displacements set to zero on the cylindrical surface and at the base. For free-swell testing, a small surcharge pressure of 0.1 MPa was applied at the top surface. For confined-swell testing, in contrast, the top surface is held at zero vertical displacement, thus holding the specimen at constant volume throughout the test. The boundary conditions for the simulated tests were selected to represent the laboratory test conditions, such as described by Hoffmann et al. [31] for wetting under constant load (free-swell testing) and wetting at constant volume (confined-swell testing). For each simulated test, the specimen was initially unsaturated with a specified suction. After mechanical initialization, the suction was reduced in small steps to a near-zero value to simulate wetting. The specimen moisture content was assumed to attain an instantaneous uniform value at each suction step and was calculated using the moisture retention relationship [Eq. (7)] for the bentonite-sand mixture and $\theta_l = r_v S_l / G_s$ where r_v is the void ratio (without accounting for r_v changes during the calculation history) and G_s is the relative density of mineral grains. Mechanical response of the specimen to the prescribed suction history was calculated using a FLAC [15] implementation of the model described in this paper. Two analyses were performed in each case: one analysis with α_{CW} set to zero, referred to as “wetting without swelling,” and a second analysis with α_{CW} set to its known value, referred to as “wetting with swelling.” The initial suction was 50 MPa and the mechanical parameters are as described in the first paragraph of Section 3.1.1. Suction was decreased in 0.05 MPa steps.

3.2.1 Results from simulated free-swell testing

The calculated yield function value F_s [Eq. (25)] from the “wetting with swelling” analysis, plotted as a function of s shows the mechanical state was elastic ($F_s < 0$) until suction decreased to

~10 MPa (Fig. 20, solid blue curve). As the figure shows, plastic yielding ($F_s \approx 0$) occurred at this value of suction and the mechanical state remained elastic-plastic during the rest of the wetting sequence. The preconsolidation pressure P_c remained constant at 17.5 MPa until the onset of plastic deformation (Fig. 20, solid red curve). The plastic deformation caused P_c to increase, due to compaction according to Eqs. (33) and (34), as s decreased to the air entry value of 2.5 MPa (compare with behavior described in Fig. 11). As s decreased further, P_c decreased and approached the value for a saturated state.

The mechanical state was elastic ($F_s < 0$) throughout the "wetting without swelling" analysis, as shown in Fig. 20 (dotted green curve). Therefore, P_c was constant at 17.5 MPa during the analysis until s decreased to the air entry value of 2.5 MPa. Further decrease in s caused P_c to decrease toward the value for a saturated state.

Plots of the p-q stress paths (Fig. 21) provide more explanation of differences in mechanical response from the "wetting with swelling" and "wetting without swelling" analyses. As the figure shows, q increased rapidly relative to p in "wetting with swelling." The lateral effective stress increased due to suppressed lateral swelling but decreased due to suction release with a net increase as the effect of swelling increased. In contrast, the axial stress decreased due to suction release but was not affected by swelling because the specimen is free to swell axially. Therefore, q increased rapidly relative to p and the p-q stress path intersected the initial yield surface at point A. Subsequently, the yield surface expanded between points A and B and contracted between points B and C. In contrast, for the "wetting without swelling" case, q was essentially constant while p decreased. The axial and lateral effective compressive stress decreased at the same rate due to suction release and there was no swelling effect. Therefore, q was essentially constant while p decreased and the p-q stress path was almost horizontal and inside of the yield surface (Fig. 21).

Axial (vertical) deformation

The calculated vertical displacement is shown in Fig. 22 for the "wetting with swelling" (blue curve) and "wetting without swelling" (red curve) analyses. The difference between the two displacements (green curve) represents deformation due to swelling. The mechanical response to wetting consists of three contributions: (1) elastic relaxation due to suction release, (2) compression due to stiffness reduction, and (3) swelling. The "wetting without swelling" analysis can include the first two contributions but not the third. As Fig. 22 (red curve) shows, the first contribution (relaxation due to suction release) was initially dominant and resulted in a net positive displacement at s values greater than ~4 MPa. As s decreased to smaller values in the "wetting without swelling" analysis, compression due to stiffness reduction became dominant and resulted in a net negative displacement. However, the overall mechanical response as obtained with the "wetting with swelling" analysis (blue curve) resulted in a net axial expansion because the swelling contribution is much greater than the other two. The calculated net deformation shows an axial expansion of ~17%. Although this analysis is not compared against any laboratory data, in a previous analysis of the bentonite-sand mixture [29], the authors showed that axial expansion calculated using the model compared well with axial expansion from laboratory oedometer free-swell testing.

Swelling pressure

The simulated test conditions permitted development of swelling pressure, because the boundary conditions did not permit the potential lateral swelling. The swelling pressure was

calculated as the difference between the effective pressure in the “wetting with swelling” and “wetting without swelling” analyses and is shown as the green curve in Fig. 23. As the figure shows, the swelling pressure increased during wetting and reached a maximum of ~6.6 MPa at a suction value near the air-entry pressure. The swelling pressure decreased with suction thereafter and approached ~1 MPa at saturation. Therefore, for this material and simulated test conditions (e.g., geometry, initial suction, mechanical properties), the analysis indicates the maximum swelling pressure that an embedded structure such as waste container could experience is greater than the swelling pressure at saturation.

3.2.2 Results from simulated confined-swell testing

The calculated F_s versus s and P_c versus s for the “wetting with swelling” and “wetting without swelling” analyses are shown in Fig. 24. Plastic yielding occurred in the first analysis at $s \approx 16$ MPa but did not result in compaction or any effect on P_c because the test conditions did not permit any volume change. Therefore, P_c was constant at 17.5 MPa until s decreased to smaller than the air-entry pressure. As s decreased further, P_c decreased and approached the value for a saturated state. For the “wetting without swelling” analysis, the mechanical state was elastic ($F_s < 0$) throughout. Therefore, P_c did not change until s decreased to smaller than the air-entry pressure.

The boundary conditions for this test did not permit any deviatoric stress. Therefore, $q = 0$, the p-q stress path is horizontal and coincident with the p axis (Fig. 10), and the behavior of the stress path can be understood using the p versus s plots (Fig. 25). As the figure shows, p decreased monotonically toward zero throughout the “wetting without swelling” analysis. In contrast, for “wetting with swelling,” p decreased initially, then increased until yielding (i.e., $p = P_c$), remained constant until s decreased to smaller than the air-entry value. Thereafter, p decreased as the yield surface contracted because of decreasing P_c.

As shown in Fig. 25, the calculated swelling pressure increased to a maximum of ~15 MPa at a suction value approximately equal to the air-entry pressure. The swelling pressure thereafter decreased toward a value of ~2.5 MPa at the saturated state. The calculated swelling pressure from the “free-swell” and confined swell tests indicate, as is expected, that swelling pressure is not a material property, but a product of mechanical conditions and properties and wetting history. Hoffmann et al. [31] arrived at a similar observation based on laboratory swelling test results for wetting under constant load (similar to the “free-swell” test condition) and wetting at constant volume (similar to the confined swell test condition).

3.3 Simulated free-swell and confined-swell testing of MX80 E-Mix granular bentonite

The simulated test geometry and boundary conditions are the same as described in Section 3.2. For each simulated test, the specimen was initially unsaturated with suction $s = 200$ MPa. After mechanical initialization, the suction was reduced in 0.05 MPa steps to a near-zero value to simulate wetting. The specimen moisture content and mechanical response were calculated as described previously (Section 3.2). Also, two analyses were performed in each case: “wetting without swelling” and “wetting with swelling.” The mechanical parameters are as described in Section 3.1.2.

3.3.1 Results from simulated free-swell testing

The calculated F_s versus s and P_c versus s for the "wetting with swelling" analysis (Fig. 26) show the mechanical state was elastic ($F_s < 0$) until suction decreased to ~95 MPa. As the figure shows, plastic yielding ($F_s \approx 0$) occurred at this value of suction and the mechanical state remained elastic-plastic during the rest of the wetting sequence. The preconsolidation pressure P_c (solid red curve) remained constant at 34.3 MPa until the onset of plastic deformation. Plastic deformation caused P_c to increase initially because of compaction. Then, as the stress condition traversed critical state (compare with Fig. 10) the volumetric strain behavior changed from compaction to dilation and P_c decreased according to Eqs. (33) and (34) as s decreased from ~24 MPa to the air entry value of 5 MPa. As s decreased further, P_c decreased and approached the value for a saturated state. In contrast, the mechanical state remained elastic throughout the "wetting without swelling" analysis (dotted green curve). Therefore, P_c remained constant at 34.3 MPa while s was greater than the air-entry value, but decreased thereafter as s decreased.

The p-q stress paths (Fig. 27) from this test are similar to the stress paths discussed previously (Fig. 21). As Fig. 27 shows for the "wetting with swelling" analysis (blue curve), q increased rapidly relative to p, starting at the onset of swelling (i.e., point of separation of the blue and red curves) until the stress path intersects the initial yield surface at point A. In the stress-path segment OA, both lateral and vertical compressive stresses decreased initially due to suction release. At the onset of swelling, the lateral compressive stress increased but the vertical continued to decrease. Therefore, q increased rapidly relative to p. Between points A and B, the yield surface expanded initially because of increase in P_c due to compaction, reached a maximum size and contracted because of decrease in P_c due to dilation. Yield surface contraction continued from point B toward C because of suction effects on P_c at s values smaller than the air-entry pressure. In contrast, for the "wetting without swelling" case, the p-q stress path was on the inside of the yield surface throughout the analysis. The value of q did increase as p decreased: Potential expansion due to suction release occurred in the vertical direction (Fig. 28, red curve) but was suppressed laterally. Therefore, the lateral compressive stress increased relative to the vertical, resulting in an increase in q. A similar increase in q occurred in the bentonite-sand mixture model (Fig. 21) but the magnitude of the increase was greater in the MX80 E-Mix granular bentonite model (Fig. 27). However, the q increase in the "wetting without swelling analysis" with either model was small such that the p-q stress path remained on the inside of the yield surface, i.e., the mechanical state was elastic throughout the analysis.

Axial (vertical) deformation

The calculated vertical displacement for this analysis (Fig. 28) has features similar to the vertical displacements in Fig. 22 that were calculated for the bentonite-sand mixture. In the "wetting without swelling" analysis, the specimen expanded axially initially until s decreased to ~11 MPa but the test ended with a net specimen compression of ~5%. In contrast, the "wetting with swelling" analysis ended with a net specimen expansion of ~42%.

Swelling pressure

The swelling pressure, calculated as the difference between the effective pressure in the "wetting with swelling" and "wetting without swelling" analyses, increased during wetting and reached a maximum of 13.8 MPa at a suction value near the air-entry pressure of 5 MPa (Fig. 29). The swelling pressure decreased with suction thereafter and approached ~3 MPa at saturation. Therefore, for this material and simulated test conditions, the analysis indicates the

maximum swelling pressure that an embedded structure such as waste container could experience is greater than the swelling pressure at saturation. The analysis with the bentonite-sand mixture model led to a similar conclusion.

3.3.2 Results from simulated confined-swell testing

The calculated F_s versus s and P_c versus s relationships (Fig. 30) show that the stress state in the "wetting with swelling" analysis satisfied the yield condition when s decreased to ~ 110 MPa. However, plastic yielding did not result in compaction or dilation and, therefore, had no effect on P_c because the test conditions did not permit any volume change. Therefore, P_c was constant at 34.3 MPa until s decreased to smaller than the air-entry pressure. As s decreased further, P_c decreased and approached the value for a saturated state. For the "wetting without swelling" analysis, the mechanical state was elastic ($F_s < 0$) throughout. Therefore, P_c did not change until s decreased to smaller than the air-entry pressure.

As discussed in Section 3.2.2 for the bentonite-sand model, $q = 0$ and the p-q stress path is horizontal and coincident with the p axis (Fig. 10) throughout the test. The behavior of the p-q stress path can be understood using the p versus s plots (Fig. 31), which shows p decreased toward zero throughout the "wetting without swelling" analysis. In contrast, for "wetting with swelling," p decreased initially, then increased until yielding (i.e., $p = P_c$), and remained constant after yielding until s decreased to smaller than the air-entry value. Thereafter, p decreased as the yield surface contracted because of decreasing P_c.

The calculated swelling pressure (Fig. 31) increased to a maximum of 29.5 MPa at a suction value approximately equal to the air-entry pressure. The swelling pressure thereafter decreased toward a value of 4.6 MPa at the saturated state. As discussed in Section 3.2.2, the results indicate, as is expected, that swelling pressure is not a material property but a product of mechanical conditions and properties and wetting history. This interpretation of the swelling pressure agrees with the Hoffmann et al. [31] observation based on laboratory swelling tests performed at conditions similar to the simulated test conditions discussed in this paper.

3.4 Bentonite column heated at the base and subjected to water infiltration at the top

In this problem, we evaluated the mechanical response of a column of MX80 E-Mix granular bentonite heated at the base and subjected to water infiltration at the top. The evaluation consisted of thermal-hydrological (TH) analyses using a code xFlo [32] and mechanical (M) analyses using FLAC [15] with the constitutive model described in Section 2. The TH and M analyses were coupled sequentially, i.e., the calculated TH response was used as input for the M analysis but the resulting mechanical response was not used in the TH model. The analysis was intended to simulate a laboratory test on a granular bentonite column with similar boundary conditions [33, 34], which could represent bentonite buffer conditions in a geologic disposal design for radioactive waste. Numerical modeling of the test was conducted as part of the D2015 phase of the DECOVALEX program [23].

In the laboratory test, the bentonite column has cylindrical cross section with diameter of 7 cm and height of 50 cm and was placed in a Teflon® cell with outer walls reinforced with semicylindrical steel shells to avoid deformation of the Teflon during the test [33, 34]. Also, the cell was restrained at the base and top, and a load cell at the top surface was used to measure the axial pressure. The test consisted of a heating-only phase for 5,000 hr. followed by an infiltration phase for 15,000 hr. The heater temperature was increased in stages as described in

[35] to a maximum of 140°C and held constant thereafter through the remaining test time (including the infiltration phase). Temperature and relative humidity were simultaneously measured at three locations: Probe 1 at 40 cm from the bottom, Probe 2 at 22 cm, and Probe 3 at 10 cm. The water intake was measured by means of an electronic load cell measurement system. A ring load cell was used to determine the axial pressure generated during the test.

TH analysis was performed to calculate the distributions of temperature, (liquid) water saturation, and gas pressure as functions of time [35] and the distributions were used as input in the mechanical analysis. The mechanical analysis model and results are described in this paper.

3.4.1 Mechanical analysis model

The bentonite column was modeled as an axisymmetric solid of radius 0.035 m and height of 0.5 m, discretized into 198 rows of cells of 14 cells per row. An additional row of relatively stiff cells was placed at the top of the assemblage to represent the load-cell and was used to calculate the axial pressure. The top row was modeled as linear elastic and was not assigned any TH variables or properties. The 198 rows representing the bentonite were modeled using the constitutive model described in Chapter 2 with material parameters described in Section 3.1.2.

All exterior boundaries of the model were held at zero normal displacement. The axis of the cylindrical solid also was restrained by implication of axisymmetric modeling. Therefore, the overall model volume could not change. However, internal deformation of the material could occur because of temperature and moisture content changes and could generate a reaction at the top row of elements representing the axial load cell. The internal deformations consist of swelling or shrinkage and thermal expansion of the bentonite. The analysis results indicate that the contribution of thermal expansion is negligible even during the heating phase. Therefore, the mechanical response of the bentonite column was controlled by swelling and shrinkage of bentonite due to moisture redistribution caused by the heat source and water infiltration.

The value of α_{CW} [eq. (37)] based on data described in Section 2.6.2 resulted in excessive axial pressure in the model. Therefore, we modified α_{CW} to introduce a variation with moisture content (θ_l) and a difference in α_{CW} values for swelling and shrinkage as described in Fig. 32. The α_{CW} versus θ_l relationships shown in Fig. 32 were chosen to result in a calculated axial pressure that reasonably matches the measured axial pressure from the laboratory experiment. Subsequent studies of the swelling and shrinkage of bentonite may lead to better understanding of swelling and swelling pressure modeling.

3.4.2 Results of thermal-hydrological model used as input to mechanical model

Spatial distributions of θ_l and temperature (T) used in the analysis are shown in Figs. 33 and 34, respectively, at times of 4527, 5413, and 17,604 hr. These times represent the end of heating-only phase, beginning of infiltration (i.e., 5000 hr.) and end of the test (20,000 hr.). Such distributions were provided at 100 time increments through TH modeling and were used as input to the mechanical model. The TH model provided liquid saturation (S_l), T, and gas pressure (u_a). The value of θ_l was calculated from S_l using $\theta_l = r_{v0} S_l / G_s$, where $G_s = 2.74$ and $r_{v0} = 0.797$ is the initial void ratio. Also, S_l was used to calculate s, χ, and K as described in Sections 2.1 and 2.3.2.

At the start of the simulation (representing the initial state in the laboratory test) $\theta_l = 0.064$ and $T = 22℃$ everywhere. Because infiltration did not start until 5000 hr., the θ_l contour plot at 4527 hr. (Fig. 33) represents thermal effects on moisture redistribution. The contours show that during the heating-only phase (first 5000 hr.) of the simulated test, moisture content increased to almost 0.1 in approximately the middle third of the specimen, remained essentially unchanged in the upper third, and decreased to as low as approximately zero in the lower third. The moisture content changes caused swelling or shrinkage of the bentonite that manifested as axial pressure changes in the laboratory experiment. As Fig. 33 shows, moisture content changes during the infiltration phase are greater than during the heating-only phase. Therefore, mechanical response of the specimen during the infiltration phase is greater than during the heating-only phase.

3.4.3 Mechanical response

Mechanical changes in the specimen consist of internal deformation due to thermal expansion and moisture-induced swelling or shrinkage. Because the specimen was constrained mechanically at all exterior boundaries, the mechanical changes resulted in an evolution of internal pressure that was monitored in the laboratory experiment using an axial-pressure load-cell at the top of the specimen. Model calculations indicate the contribution of thermal expansion to the overall mechanical response is negligible. For example, the maximum axial pressure change due to thermal expansion is approximately 0.05 MPa, with thermal expansion modeled using a constant thermal expansivity of 10^{-5} /°C. In contrast, the measured axial pressure reached a maximum of approximately 1.5 MPa. Therefore, the mechanical response due to swelling and shrinkage caused by moisture redistribution is much greater than the effects of thermal expansion, such that the calculated response could be explained by comparing with the moisture content changes.

The spatial distributions of volumetric strain (Fig. 35) indicate dilation in approximately the middle third of the specimen during the heating-only phase (4527-hr results), which was compensated by compression in the lower and upper thirds. The dilation zone at 4527 hr. (Fig. 35) corresponds approximately to the zone of increased moisture content at 4527 hr. (Fig. 33). The results indicate that bentonite swelling in the middle third caused an increase in volume that was compensated by volume decrease in the upper and lower thirds. The onset of water infiltration at the top of the specimen resulted in a zone of increased moisture content at the top (Fig. 33, 5413 hr.) and a corresponding dilation zone at the same location (Fig. 35, 5413 hr.). The middle and upper dilation zones grew and eventually merged as shown in Fig. 35 (17,604 hr.), thus indicating specimen dilation in approximately the upper half, compensated by compression in the lower half.

The measured axial pressure (Fig. 36) was in the range of 0.1–0.2 MPa during the heating-only phase, increased rapidly to approximately 1.2 MPa at the beginning of infiltration and more gradually thereafter to a steady maximum of approximately 1.5 MPa. The calculated axial pressure histories for three model cases are compared with the measured axial pressure in Fig. 36. The axial pressure depends on the bulk modulus (K) and swelling or shrinkage coefficient (α_{CW}). The bulk modulus for each of the model cases shown in Fig. 36 varied with suction in the range of $20 \leq K \leq 50$ MPa based on the model described in Section 2.3.2 and Fig. 9 (red curve). The model cases differ only with respect to the ratio of the α_{CW} values for shrinkage relative to the values for swelling. The ratio equals 0.5 for the green curve, 0.75 for the red curve, and 1.0 for the purple curve.

Although the calculated axial pressure during the thermal and infiltration phases matches the overall trends of the measured pressure, the rapid increase in the measured axial pressure at the start of the infiltration and more gradual increase thereafter to a steady maximum were not captured by the model results. Part of the difference between the observed and calculated axial pressure response can be attributed to the differences in moisture distribution between observations and xFlo results. The xFlo calculations consistently underpredict the measured cumulative mass inflow by approximately 10 percent throughout the infiltration period, affecting total change in moisture content within the column. The time history of the measured RH also suggests that the xFlo-calculated wetting front is sharper than the observed wetting front (measured moisture changes occur deeper in the column than calculated moisture changes) [35]. In addition, temperature transients measured at the probe nearest the heater (e.g., diurnal and seasonal changes in laboratory temperature, and changes in heater temperature and insulation) were associated with axial pressure transients up to 0.006 to 0.007 MPa/°C. Further calibration of the mechanical parameters relevant to swelling pressure may yield a better match to the experiment, but additional calibration may be less important for repository conditions that feature a slow and relatively uniform buffer rewetting given the large interface area of the surrounding buffer.

4 Concluding Remarks

This paper illustrates an implementation of the Bishop principle of effective stress in constitutive modeling of unsaturated expansive soils. The implementation uses the moisture retention characteristic curve to evaluate the Bishop parameter χ and, therefore, suction contribution to the effective stress, i.e, suction pressure p_s. Although the proposed general approach provides for flexibility in χ-S_e relationships through the a_{bs} parameter, the two materials evaluated in the paper were modelled using $\chi = S_e$ (i.e., $a_{bs} = 1$). Therefore, the a_{bs} parameter was not evaluated in detail, except for the observation based on p_s-s relationships for MX80 E-Mix granular bentonite that needs $a_{bs} \leq 1.5$ for p_s to increase monotonically with s. Using the moisture retention curve as described implies p_s is defined by the hydrologic response and establishes an important hydrologic input to modeling the mechanical behavior of unsaturated soils.

Using the moisture retention characteristic curve to evaluate χ and p_s enables an evaluation of suction effects on soil strength (through the preconsolidation pressure, P_c) and stiffness (through the bulk modulus, K) without needing additional information. This approach, therefore, reduces the number of independent parameters needed in the constitutive model and allows for consistency among mechanical and thermal-hydrological modeling. That is, the moisture retention curve used for thermal-hydrological modeling is also a controlling input to mechanical modeling. Additionally, this paper describes the use of numerically simulated oedometer compression testing to augment laboratory data defining suction effects on the soil compression characteristic curve.

The approach to modeling swelling described in this paper allows the effects of mechanical boundary conditions and moisture content change and its spatial gradients to be incorporated in the analysis of swelling and swelling pressure. The basic material characteristic input is the unit swelling potential α_{CW}, which represents the volumetric strain increment per unit change in moisture content for a soil element that is free to swell in every direction. Based on this definition, using the oedometer “free-swell” test to evaluate α_{CW} likely results in underestimating the potential swelling and swelling pressure because, as discussed in Section 3.2, the

oedometer specimen is not free to swell in every direction. However, the oedometer “free-swell” test provides a better estimate of α_{CW} than other available testing techniques. Therefore, using this α_{CW} in the modeling approach described in this paper provides a good basis for estimating potential swelling and swelling pressure in a soil mass subjected to arbitrary mechanical boundary conditions and wetting history. Results calculated using the model indicate that the potential swelling pressure in a given design would vary with saturation and the maximum swelling pressure could be substantially greater than the swelling pressure in a saturated state. Furthermore, different mechanical boundary conditions could result in a substantially different swelling pressure for a given saturation. For example, the maximum swelling pressure for a constant-volume condition could be much greater than the maximum swelling pressure for other conditions that permit swelling in one or more directions.

The illustrative examples include numerical modeling of a laboratory test on a column of bentonite soil heated at the base and subjected to water infiltration at the top. Results from the model were evaluated by comparing measured and calculated axial pressure histories at the top of the specimen. The results show the proposed approach is suitable for modeling the mechanical response of swelling soils that may experience changes in saturation and temperature. However, better understanding is needed of the swelling and shrinkage potentials and their dependence on moisture content.

Acknowledgment

This paper describes work performed by the Center for Nuclear Waste Regulatory Analyses (CNWRA®) for the U.S. Nuclear Regulatory Commission (NRC) under Contract No. NRC–HQ–12–C–02–0089. The activities reported here were performed on behalf of the NRC Office of Nuclear Material Safety and Safeguards, Division of Spent Fuel Management. This paper is an independent product of the CNWRA and does not necessarily reflect the view or regulatory position of NRC. The NRC staff views expressed herein are preliminary and do not constitute a final judgment or determination of the matters addressed or of the acceptability of any licensing action that may be under consideration at NRC. The authors thank A. Ramos for document processing and G. Wittmeyer and D. Pickett for internal reviews of the manuscript. The Column Test experiment (Section 3.4) has received funding from the European Atomic Energy Community's Seventh Framework Programme (FP7/2007-2011) under grant agreement n° 249681. Modeling work described in Section 3.4 was performed in conjunction with the DECOVALEX-2015 collaborative project, Task B1.

Bibliography

[1] SKB, "Long-term safety for the final repository at Forsmark: Main report of the SR-Site project. SKB Technical Report TR-11-01," Svensk Kärnbränslehantering AB, Stockholm, 2011.

[2] Nagra, "Project Opalinus Clay Safety Report. Demonstration of disposal feasibility for spent fuel, vitrified high-level waste and long-lived intermediate-level waste (Entsorgungsnachweis). Technical Report 02-05," 2002. [Online]. Available: http://static.ensi.ch/1314108739/nagra_entsorgungsnachweis.pdf. [Accessed 29 July 2014].

[3] Andra, "Dossier 2005 Argile. Synthesis: Evaluation of the feasibility of a geological repository in an argillaceous formation. Meuse/Haute-Marne site," Andra, Paris, 2005.

[4] K. Terzaghi, R. Peck and G. Mesri, Soil Mechanics in Engineering Practice, Third Edition, New York: John Wiley & Sons, Inc., 1996.

[5] E. Alonso, A. Gens and A. Josa, "A Constitutive Model for Partially Saturated Soils," *Geotechnique,* vol. 40, no. 3, pp. 405-430, 1990.

[6] A. Bishop, "The Principle of Effective Stress," *Teknisk Ukeblad,* vol. 39, pp. 859-863, 1959.

[7] A. Bishop and G. Blight, "Some Aspects of Effective Stress in Saturated and Partly Saturated Soils," *Geotechnique,* vol. 13, no. 3, pp. 177-197, 1963.

[8] D. Fredlund and H. Rahardjo, Soil Mechanics for Unsaturated Soils, New York: John Wiley & Sons, Inc., 1993.

[9] H. Q. Pham, D. G. Fredlund and S. L. Barbour, "A study of hysteresis models for soil-water characteristic curves," *Canadian Geotechnical Journal,* vol. 42, no. 6, pp. 1548-1568, 2005.

[10] M. V. Villar, M. Sanchez and A. Gens, "Behaviour of a bentonite barrier in the laboratory: experimental results up to 8 years and numerical simulation," *Physics and Chemistry of the Earth Parts A/B/C,* vol. 33, no. Supplement 1, pp. S476-S485, 2008.

[11] W. Ye, M. Wan, B. Chen, Y. Chen, Y. Cui and J. Wang, "Effect of temperature on soil-water characteristics and hysteresis of compacted Gaomiaozi bentonite," *Journal of Central South University of Technology, English Edition,* vol. 16, no. 5, pp. 821-826, 2009.

[12] A. Seiphoori, A. Ferrari and L. Laloui, "An Insight Into the Water Retention Behaviour of MX 80 Granular Bentonite," in *International Conference on the Performance of Engineered Barriers*, Hannover, Germany, 2014.

[13] M. Ajdari, G. Habibagahi, H. Nowamooz, F. Masrouri and A. Ghahramani, "Shear Strength Behavior and Soil Water Retention Curve of a Dual Porosity Silt-Bentonite Mixture," *Scientia Iranica,* vol. 17, no. 6, pp. 430-440, 2010.

[14] J. Rutqvist, Y. Ijiri and H. Yamamoto, "Implementation of the Barcelona Basic Model in TOUGH-FLAC for Simulations of the Geomechanical Behavior of Unsaturated Soils," *Computers & Geosciences,* vol. 37, pp. 751-762, 2011.

[15] Itasca Consulting Group, "FLAC Version 7.0, Fast Lagrangian Analysis of Continua, User's Guide," Itasca Consulting Group, Minneapolis, Minnesota, 2011.

[16] M. Nuth and L. Laloui, "Advanced Hydro-Mechanical Coupling for Unified Constitutive Modeling of Unsaturated Soils," in *Unsaturated Soils: Advances in Geo-Engineering*, London, UK, Taylor & Francis Group, 2008, pp. 559-565.

[17] N. Lu, "Interpreting The "Collapse" Behavior of Unsaturated Soil By Effective Stress Principle," in *Multiscale and Multiphysics Processes in Geomechanics*, Berlin, Springer-Verlag, 2011, pp. 81-84.

[18] D. Systemes, "ABAQUS User Manual Version 6.11," SIMULIA, A Division of Dassault Systemes, Providence, Rhode Island, 2011.

[19] J. Pereira and E. Alonso, "Insights into the links between microstructure and Bishop's parameter for unsaturated soils," in *4th Asia-Pacific Conference on Unsaturated Soils*, Newcastle, Australia, 2009.

[20] Q. Wang, Y.-J. Cui, A. Tang, J. Barnichon, S. Saba and W.-M. Ye, "Hydraulic conductivity and microstructure changes of compacted bentonite/sand mixture during hydration," *Engineering Geology,* vol. 164, pp. 67-76, August 2013.

[21] Q. Wang, A. M. Tang, Y. -J. Cui, P. Delage, J. -D. Barnichon and W. -M. Ye, "The Effects of Technological Voids on the Hydro-Mechanical Behaviour of Compacted Bentonite-Sand Mixture," *Soils and Foundations,* vol. 53, no. 2, pp. 232-245, 2013.

[22] M. Rizzi, A. Seiphoori, A. Ferrari, D. Ceresetti and L. Laloui, "Analysis of the Behaviour of the Granular MX-80 Bentonite in THM-Processes," Nagra: National Cooperative for the Disposal of Radioactive Waste, Wettingen, Switzerland, 2012.

[23] DECOVALEX, "DECOVALEX," 2014. [Online]. Available: http://www.decovalex.org/. [Accessed 16 March 2015].

[24] M. van Genuchten, "A Closed-Form Equation for Predicting the Hydraulic Conductivity of Unsaturated Soils," *Soil Sci. Soc. ,* vol. 44, pp. 892-898, 1980.

[25] C. Desai and H. Siriwardane, Constitutive Laws for Engineering Materials with Emphasis on Geologic Materials, Englewood Cliffs, New Jersey: Prentice-Hall, Inc., 1984.

[26] K. Bathe, Finite Element Procedures in Engineering Analysis, Englewood Cliffs, New Jersey: Prentice-Hall, Inc., 1983.

[27] S. Agus and T. Schanz, "A Method for Predicting Swelling Pressure of Compacted Bentonites," *Acta Geotechnica,* vol. 3, pp. 125-137, 2008.

[28] G. Montes-H, J. Duplay, L. Martinez, Y. Geraud and B. Rousset-Tournier, "Influence of Interlayer Cations on the Water Sorption and Swelling-Shrinkage of MX80 Bentonite," *Applied Clay Science,* vol. 23, pp. 309-321, 2003.

[29] G. Ofoegbu, B. Dasgupta, C. Manepally, H. Basagaoglu and R. Fedors, "Modeling Swelling and Swelling Pressure in Expansive Clays," in *2013 International High-Level Radioactive Waste Management Conference*, Albuquerque, New Mexico, 2013.

[30] H. Nowamooz and F. Masrouri, "Influence of Suction Cycles on the Soil Fabric of Compacted Swelling Soil," *Comptes Rendus Geoscience,* vol. 342, pp. 901-910, 2010.

[31] C. Hoffmann, E. Alonso and E. Romero, "Hydro-mechanical behaviour of bentonite pellet mixtures," *Physics and Chemistry of the Earth,* vol. 32, pp. 832-849, 2007.

[32] S. Painter, "xFlo Version 1.0 Beta User's Manual," Center for Nuclear Waste Regulatory Analyses, San Antonio, TX, 2006.

[33] M. V. Villar, P. Martin, R. Gomez-Espina, F. Romero and J. Barcala, "THM Cells for the HE-E Test: Setup and First Results," PEBS, Long-term Performance of Engineered Barrier Systems, Madrid, Spain, 2012.

[34] M. Villar, P. Martin, R. Gomez-Espina and F. Romero, "Long-term THM Tests Reports: THM Cells for the HE-Test: Update of Results Until February 2014. PEBS Report D2.2-7.3.," Long-Term Performance of Engineered Barriers Systems Project, Madrid, Spain, 2014.

[35] Manepally, C., S. Stothoff, G. Ofoegbu, B. Dasgupta, and R. Fedors,, " Modeling Thermohydrological-Mechanical Behavior of Granular Bentonite, " in *2013 International High-Level Radioactive Waste Management Conference*, Charleston, South Carolina, 2015.

List of Figure Captions

Fig. 1 Bishop parameter versus effective saturation (χ-S_e) relationships based on Eq. (5) and showing the effects of the a_{bs} fitting parameter

Fig. 2 Moisture retention relationships for a bentonite-sand mixture based on reference [20] data and Eq. (7) curve-fitting

Fig. 3 Bishop parameter versus suction (χ-s) relationships for the bentonite-sand mixture described in Fig. 2 showing the effects of the a_{bs} fitting parameter

Fig. 4 Suction pressure (i.e., suction contribution to the effective pressure) versus suction (p_s-s) relationships for the bentonite-sand mixture described in Fig. 2 showing the effects of the a_{bs} fitting parameter

Fig. 5 Moisture retention relationships for MX80 E-Mix granular bentonite based on reference [22] data and Eqs. (8) and (9) curve-fitting

Fig. 6 Bishop parameter versus suction (χ-s) relationships for MX80 E-Mix granular bentonite described in Fig. 5 showing the effects of the a_{bs} fitting parameter

Fig. 7 Suction pressure (i.e., suction contribution to the effective pressure) versus suction (p_s-s) relationships for MX80 E-Mix granular bentonite described in Fig. 5 showing the effects of the a_{bs} fitting parameter

Fig. 8 Schematic soil compression characteristic curve based on a bilinear μ- $\log p$ relationship

Fig. 9 Bulk modulus versus suction (K-s) relationships for MX80 E-Mix granular bentonite based on Eq. (20) and showing the effects of K_∞ and assumptions regarding minimum bulk modulus (K_inf = K_∞, w0 = w_0, PC = preconsolidation, and REF = reference)

Fig. 10 Schematic illustration of the generalized q-p yield surface [Eq. (25)] for unsaturated soil

Fig. 11 Suction contribution to preconsolidation pressure, P_{cs} versus s for MX80 E-Mix granular bentonite showing changes during drainage and imbibition (from a hypothetical maximum suction)

Fig. 12 Laboratory oedometer compression curves for the bentonite-sand mixture based on reference [20] data

Fig. 13 Reference specific volume versus suction (μ_{ref0}-s) relationships for the bentonite-sand mixture based on reference [20] data curve-fitting

Fig. 14 Unloading/reloading slope versus suction (κ_r-s) and normal-compression slope versus suction (λ_s-s) relationships for the bentonite-sand mixture based on matching numerically simulated compression test results with the laboratory data (Fig. 12)

Fig. 15 Swelling strain versus moisture content for the bentonite-sand (based on [36]) and granular bentonite (based on [22]) mixtures. Note that the numbers in this figure

represent absolute fractions: The granular bentonite experienced several hundred percent swelling at several hundred percent moisture content. The bentonite-sand, in contrast, experienced up to 20 percent swelling at up to 30 percent moisture content. We used the gradient of the strain versus moisture content relationship to evaluate the unit swelling potential

Fig. 16 Simulated oedometer compression test on the bentonite-sand mixture for $s = 12.6$ MPa compared with reference [20] laboratory test data

Fig. 17 Value of effective pressure p for a given specific volume μ on the normal-compression segment of the oedometer compression curve, based on numerically simulated testing of the bentonite-sand mixture. Dashed segments indicate minimum acceptable relationships, whereas the solid curves represent the relationships calculated by honoring reference [36] laboratory test data

Fig. 18 Simulated oedometer compression test results for MX80 E-Mix granular bentonite and laboratory data from $s = 0$ testing from reference [22]

Fig. 19 Value of effective pressure p for a given specific volume μ on the normal-compression segment of the oedometer compression curve, based on numerically simulated testing of MX80 E-Mix granular bentonite

Fig. 20 Variation of the yield function value F_s and the preconsolidation pressure P_c based on numerically simulated oedometer free-swell testing of the bentonite-sand mixture, subjected to progressive wetting to saturation from an initial suction of 50 MPa

Fig. 21 Calculated p-q stress paths based on Eqs. (22) and (23) from the simulated free-swell testing of bentonite-sand mixture described in Fig. 25. Path OABC represents the general direction of the simulated tests

Fig. 22 Calculated axial displacement versus suction from the simulated free-swell testing of bentonite-sand mixture described in Fig. 25

Fig. 23 Calculated effective pressure versus suction showing the effect of wetting on swelling pressure from the simulated free-swell testing of bentonite-sand mixture described in Fig. 25

Fig. 24 Variation of the yield function value F_s and the preconsolidation pressure P_c based on numerically simulated oedometer confined (i.e., constant volume) swell testing of the bentonite-sand mixture, subjected to progressive wetting to saturation from an initial suction of 50 MPa

Fig. 25 Calculated effective pressure versus suction showing the effect of wetting on swelling pressure from the simulated constant-volume swell testing of bentonite-sand mixture described in Fig. 29

Fig. 26 Variation of the yield function value F_s and the preconsolidation pressure P_c based on numerically simulated oedometer free-swell testing of MX80 E-Mix granular bentonite, subjected to progressive wetting to saturation from an initial suction of 200 MPa

Fig. 27 Calculated p-q stress paths based on Eqs. (22) and (23) from the simulated free-swell testing of granular bentonite described in Fig. 31. Path OABC represents the general direction of the simulated tests

Fig. 28 Calculated axial displacement versus suction from the simulated free-swell testing of granular bentonite described in Fig. 31

Fig. 29 Calculated effective pressure versus suction showing the effect of wetting on swelling pressure from the simulated free-swell testing of granular bentonite described in Fig. 31

Fig. 30 Variation of the yield function value F_s and the preconsolidation pressure P_c based on numerically simulated oedometer confined (i.e., constant volume) swell testing of MX80 E-Mix granular bentonite, subjected to progressive wetting to saturation from an initial suction of 200 MPa

Fig. 31 Calculated effective pressure versus suction showing the effect of wetting on swelling pressure from the simulated constant-volume swell testing of granular bentonite described in Fig. 35

Fig. 32 Relationships between unit swelling/shrinkage potential (α_{CW}) and moisture content (θ_l) used in the numerical modeling example described in Section 3.4.

Fig. 33 Typical spatial distributions of moisture content (θ_l) used as input to the numerical modeling example described in Section 3.4. The test column is 0.035 m wide by 0.5 m high.

Fig. 34 Typical spatial distributions of temperature (T) used as input to the numerical modeling example described in Section 3.4. The test column is 0.035 m wide by 0.5 m high.

Fig. 35 Calculated spatial distributions of volumetric strain in the modeled bentonite column based on the numerical modeling example described in Section 3.4. The test column is 0.035 m wide by 0.5 m high.

Fig. 36 Calculated histories of axial pressure at the top of the bentonite column compared with the measured axial pressure, based on the numerical modeling example described in Section 3.4.

Table 1. Slope parameters of the soil compression characteristic curve for the bentonite-sand mixture based on numerically simulated oedometer compression testing

Suction (MPa)	κ_r	λ_s
0	0.05	0.12
4.2	0.038	0.15
12.6	0.035	0.17
38.0	0.025	0.21

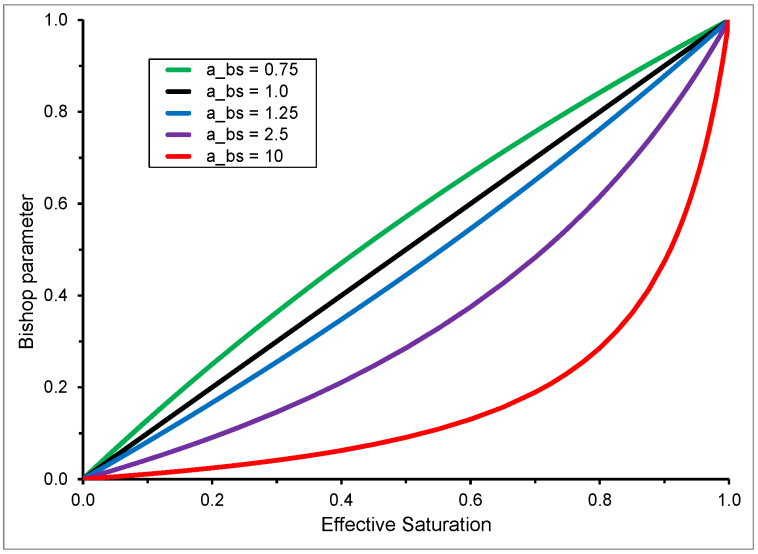

Fig. 1. Bishop parameter versus effective saturation (χ-S_e) relationships based on Eq. (5) and showing the effects of the a_{bs} fitting parameter

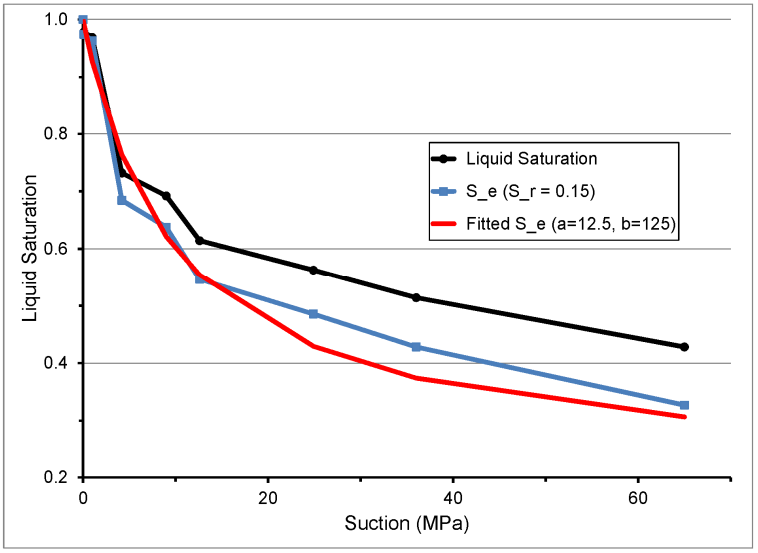

Fig. 2. Moisture retention relationships for a bentonite-sand mixture based on reference [20] data and Eq. (7) curve-fitting

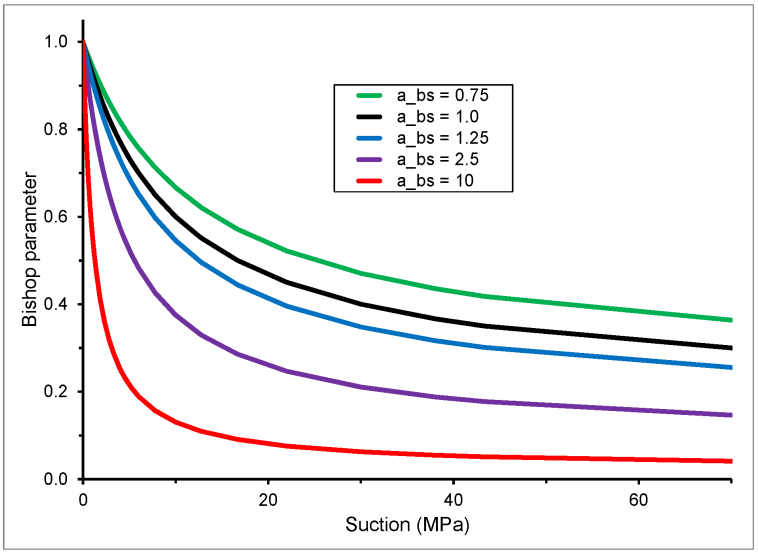

Fig. 3. Bishop parameter versus suction (χ-s) relationships for the bentonite-sand mixture described in Fig. 2 showing the effects of the a_{bs} fitting parameter

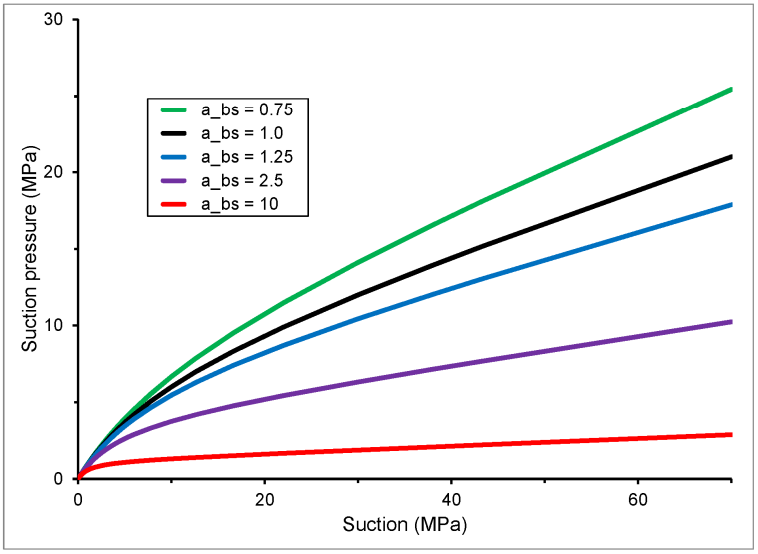

Fig. 4. Suction pressure (i.e., suction contribution to the effective pressure) versus suction (p_s-s) relationships for the bentonite-sand mixture described in Fig. 2 showing the effects of the a_{bs} fitting parameter

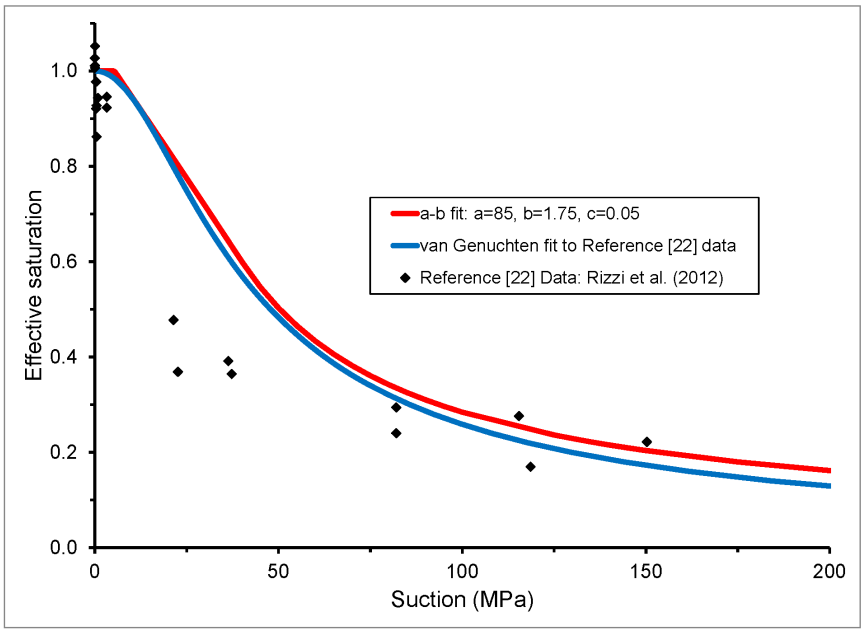

Fig. 5. Moisture retention relationships for MX80 E-Mix granular bentonite based on reference [22] data and Eqs. (8) and (9) curve-fitting

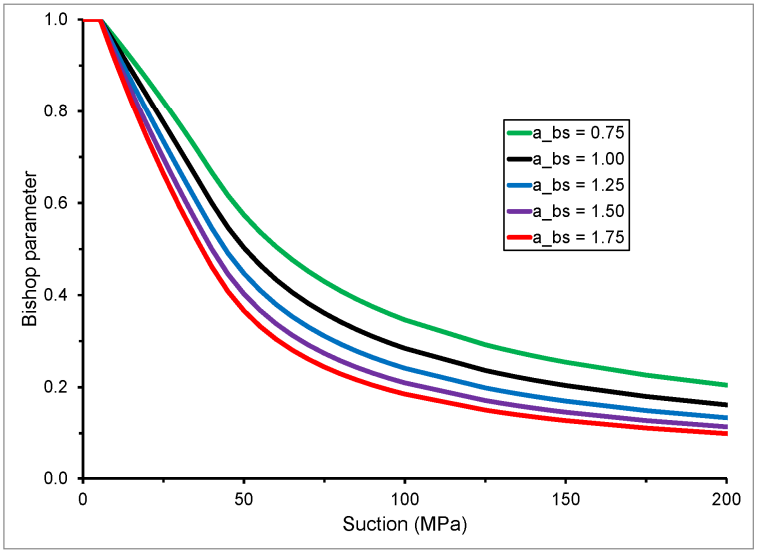

Fig. 6. Bishop parameter versus suction (χ-s) relationships for MX80 E-Mix granular bentonite described in Fig. 5 showing the effects of the a_{bs} fitting parameter

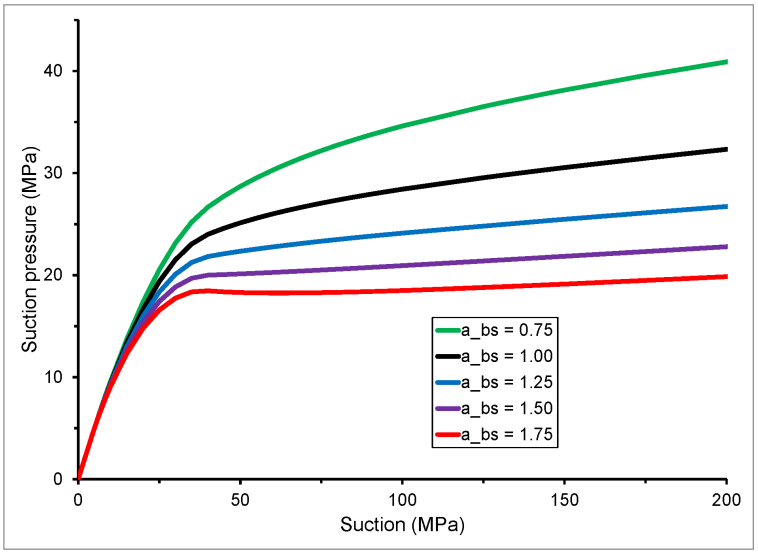

Fig. 7. Suction pressure (i.e., suction contribution to the effective pressure) versus suction (p_s-s) relationships for MX80 E-Mix granular bentonite described in Fig. 5 showing the effects of the a_{bs} fitting parameter

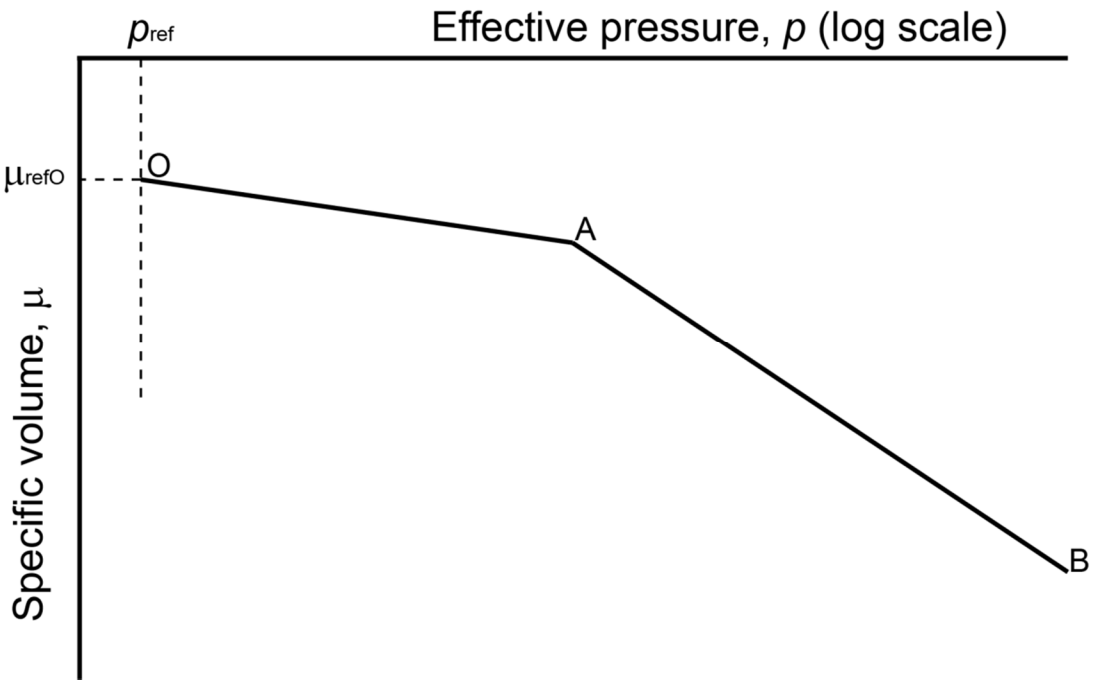

Fig. 8. Schematic soil compression characteristic curve based on a bilinear μ- $\log p$ relationship

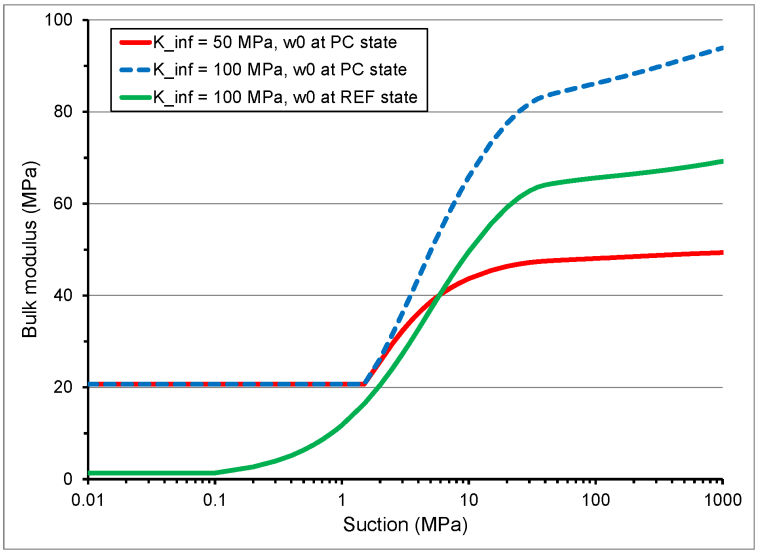

Fig. 9. Bulk modulus versus suction (K-s) relationships for MX80 E-Mix granular bentonite based on Eq. (20) and showing the effects of K_∞ and assumptions regarding minimum bulk modulus (K_inf = K_∞, w0 = w_0, PC = preconsolidation, and REF = reference)

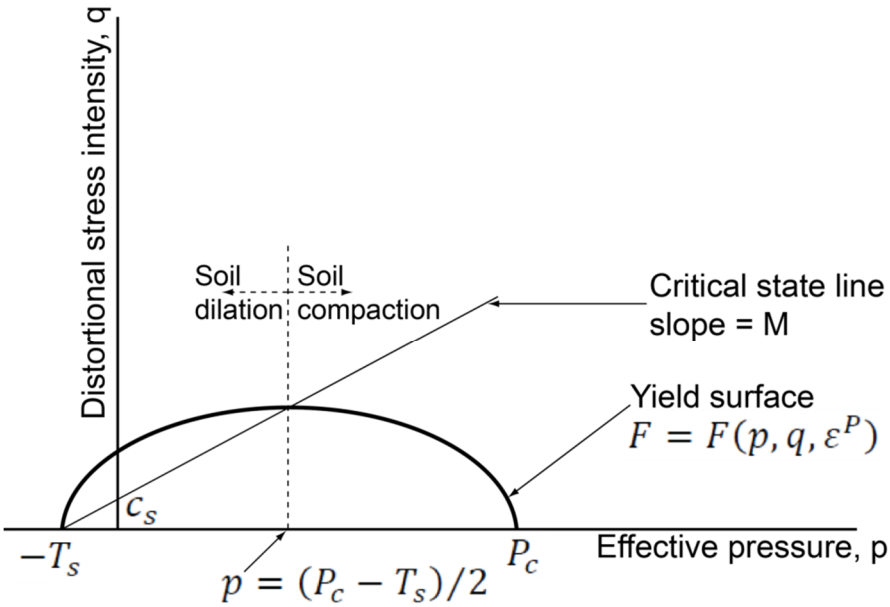

Fig. 10. Schematic illustration of the generalized q-p yield surface [Eq. (25)] for unsaturated soil

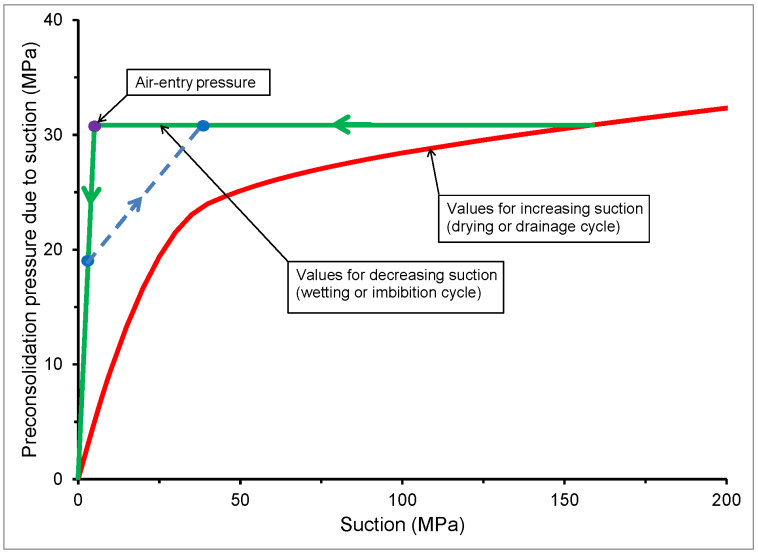

Fig. 11. Suction contribution to preconsolidation pressure, P_{cs} versus s for MX80 E-Mix granular bentonite showing changes during drainage and imbibition (from a hypothetical maximum suction)

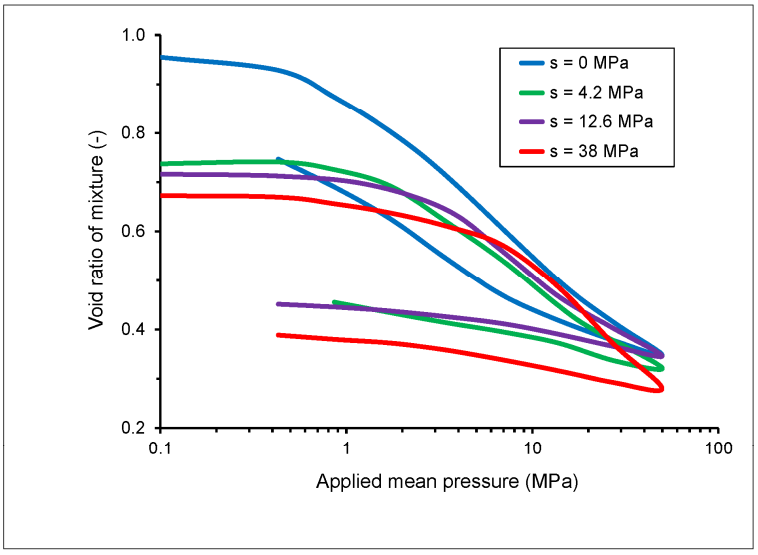

Fig. 12. Laboratory oedometer compression curves for the bentonite-sand mixture based on reference [20] data

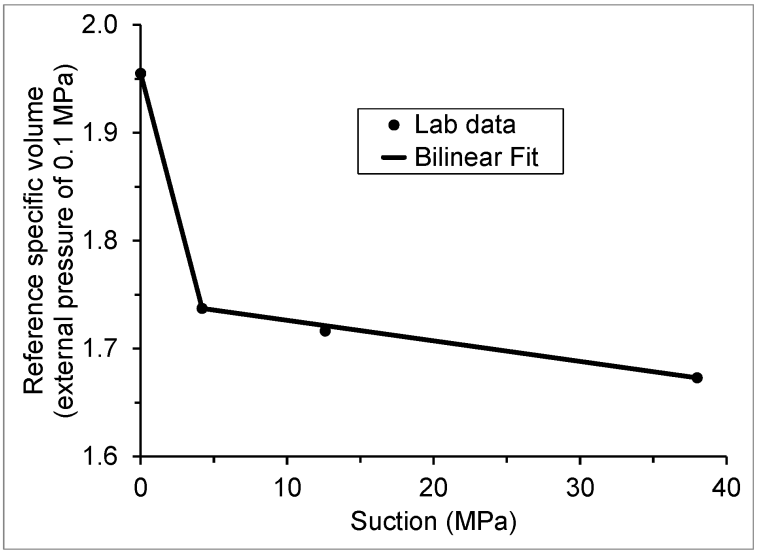

Fig. 13. Reference specific volume versus suction (μ_{refO}-s) relationships for the bentonite-sand mixture based on reference [20] data curve-fitting

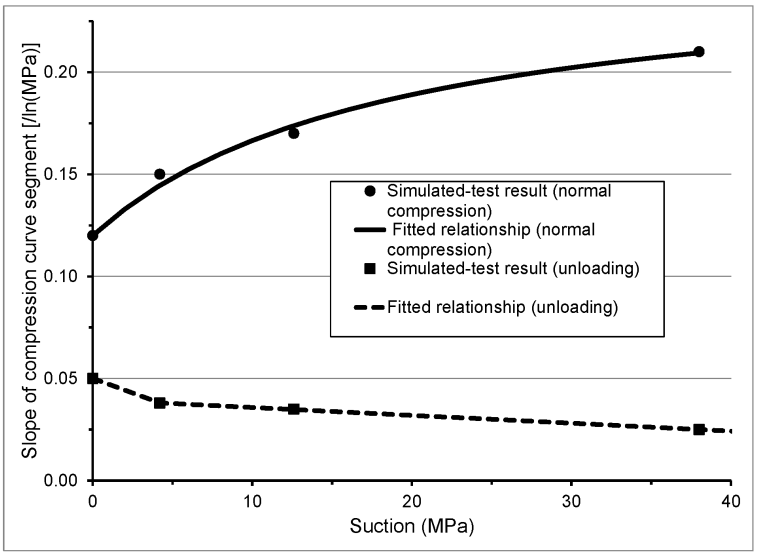

Fig. 14. Unloading/reloading slope versus suction (κ_r-s) and normal-compression slope versus suction (λ_s-s) relationships for the bentonite-sand mixture based on matching numerically simulated compression test results with the laboratory data (Fig. 12)

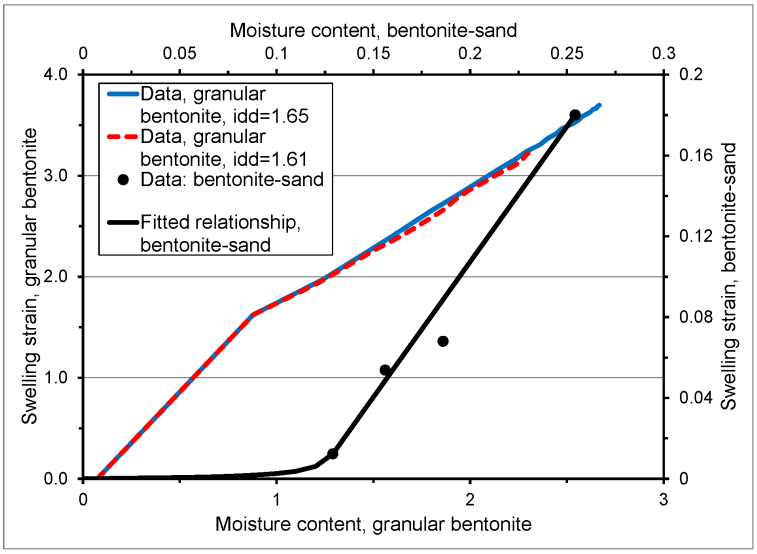

Fig. 15. Swelling strain versus moisture content for the bentonite-sand (based on [36]) and granular bentonite (based on [22]) mixtures ("idd" in the legend stands for "initial dry density"). We used the gradient of the strain versus moisture content relationship to evaluate the unit swelling potential

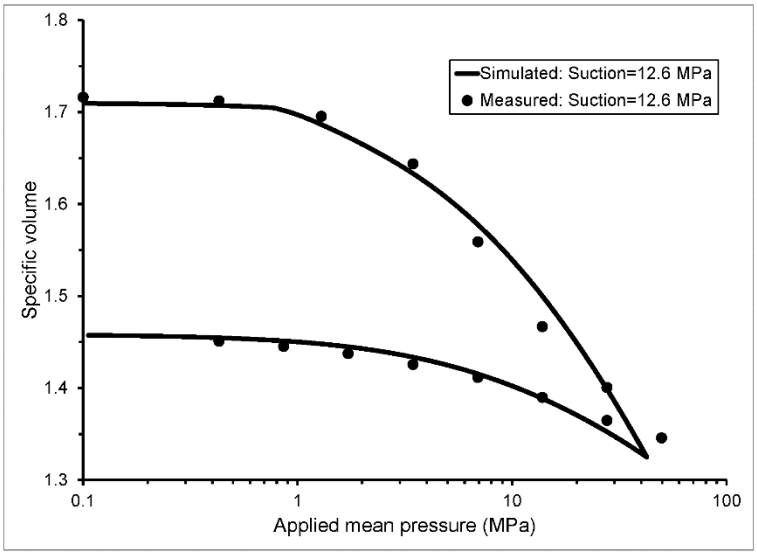

Fig. 16. Simulated oedometer compression test on the bentonite-sand mixture for $s = 12.6$ MPa compared with reference [20] laboratory test data

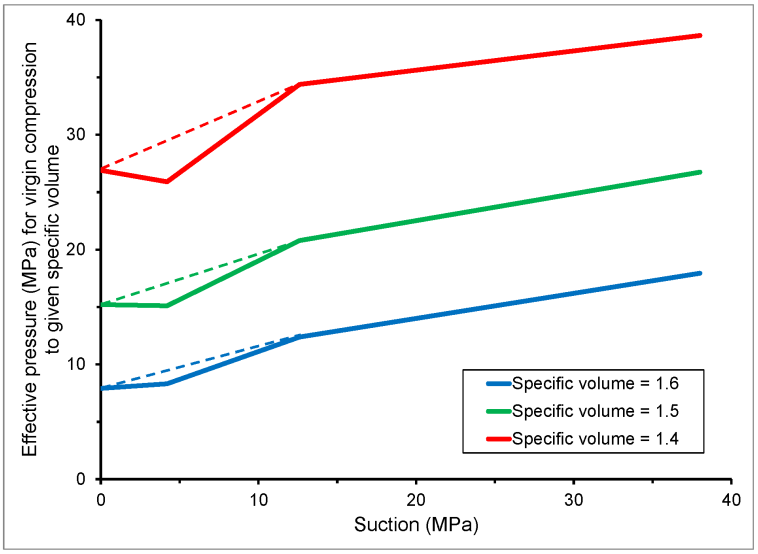

Fig. 17. Value of effective pressure p for a given specific volume μ on the normal-compression segment of the oedometer compression curve, based on numerically simulated testing of the bentonite-sand mixture. Dashed segments indicate minimum acceptable relationships, whereas the solid curves represent the relationships calculated by honoring reference [36] laboratory test data

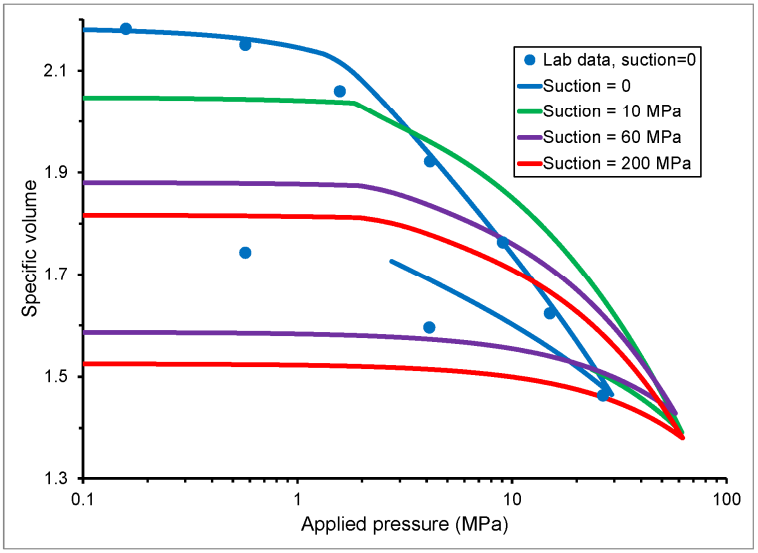

Fig. 18. Simulated oedometer compression test results for MX80 E-Mix granular bentonite and laboratory data from $s = 0$ testing from reference [22]

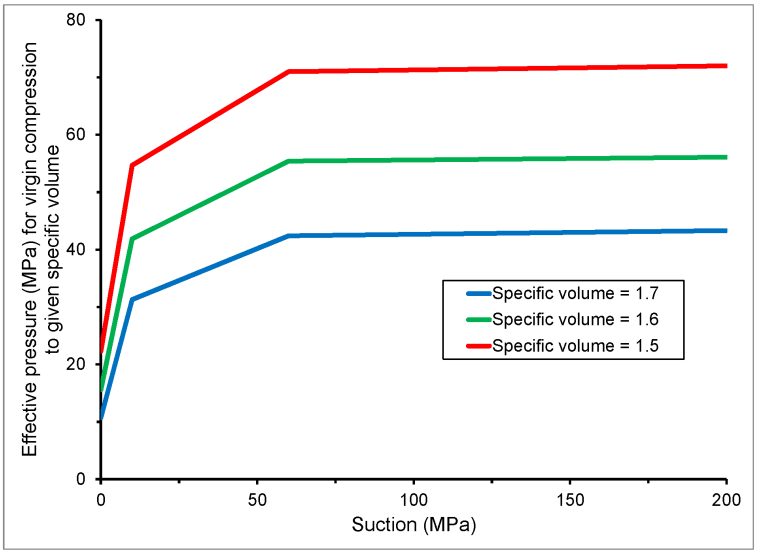

Fig. 19. Value of effective pressure p for a given specific volume μ on the normal-compression segment of the oedometer compression curve, based on numerically simulated testing of MX80 E-Mix granular bentonite

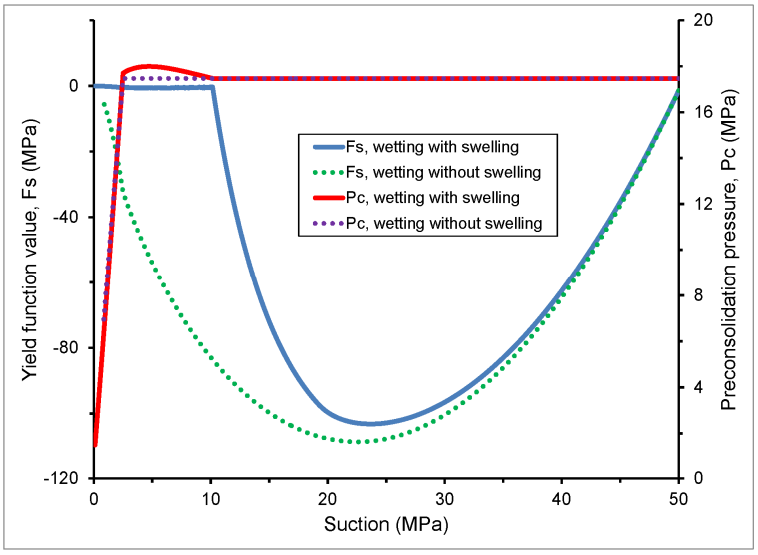

Fig. 20. Variation of the yield function value F_s and the preconsolidation pressure P_c based on numerically simulated oedometer free-swell testing of the bentonite-sand mixture, subjected to progressive wetting to saturation from an initial suction of 50 MPa

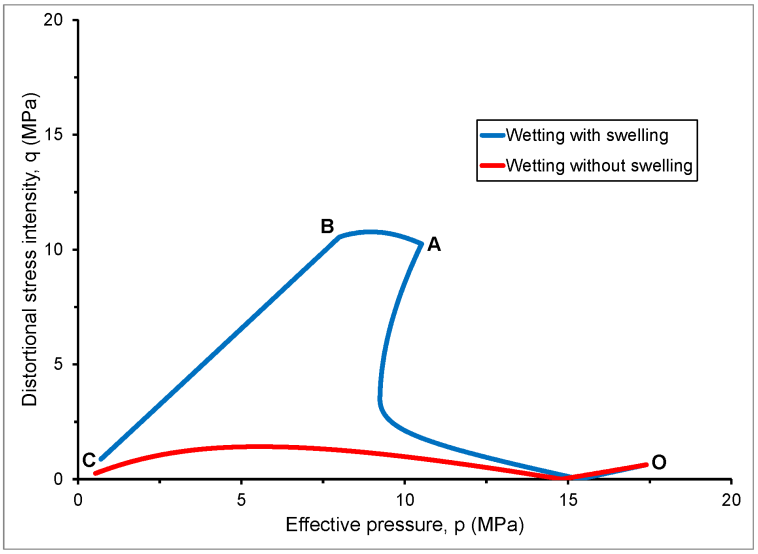

Fig. 21. Calculated p-q stress paths based on Eqs. (22) and (23) from the simulated free-swell testing of bentonite-sand mixture described in Fig. 25. Path OABC represents the general direction of the simulated tests

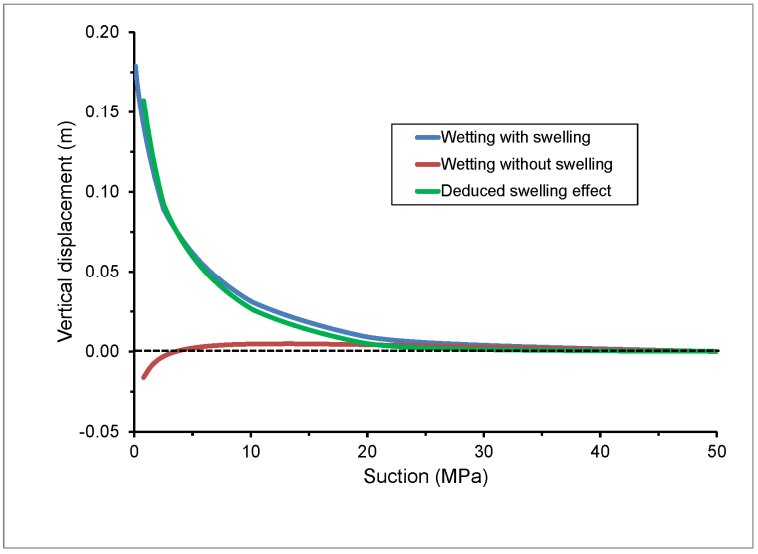

Fig. 22. Calculated axial displacement versus suction from the simulated free-swell testing of bentonite-sand mixture described in Fig. 25

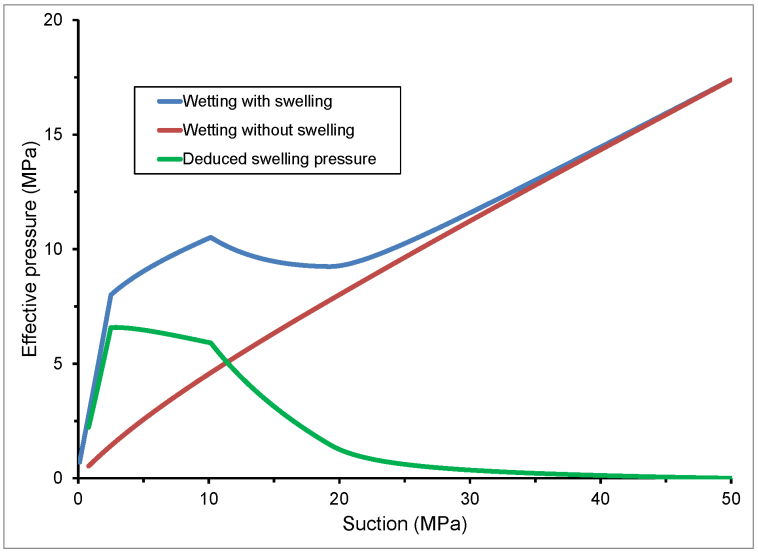

Fig. 23. Calculated effective pressure versus suction showing the effect of wetting on swelling pressure from the simulated free-swell testing of bentonite-sand mixture described in Fig. 25

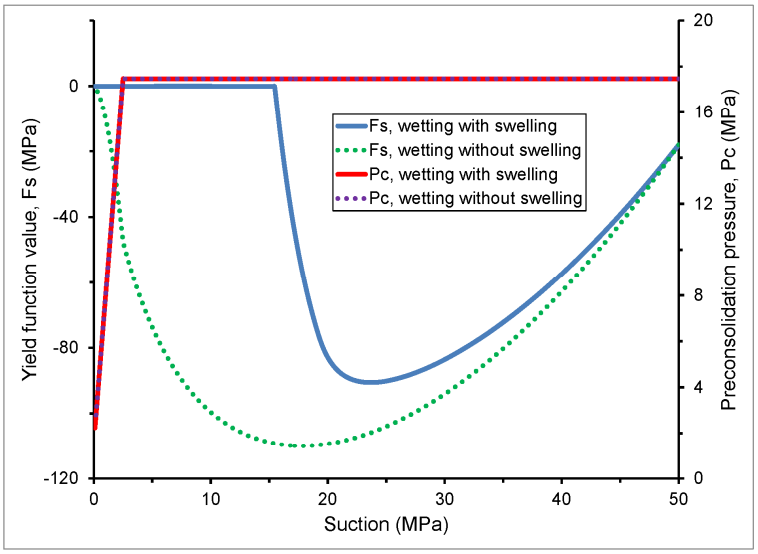

Fig. 24. Variation of the yield function value F_s and the preconsolidation pressure P_c based on numerically simulated oedometer confined (i.e., constant volume) swell testing of the bentonite-sand mixture, subjected to progressive wetting to saturation from an initial suction of 50 MPa

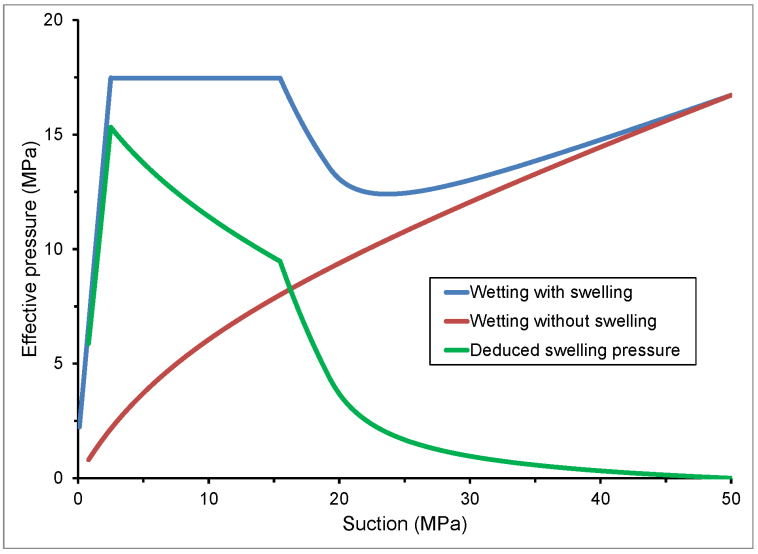

Fig. 25. Calculated effective pressure versus suction showing the effect of wetting on swelling pressure from the simulated constant-volume swell testing of bentonite-sand mixture described in Fig. 29

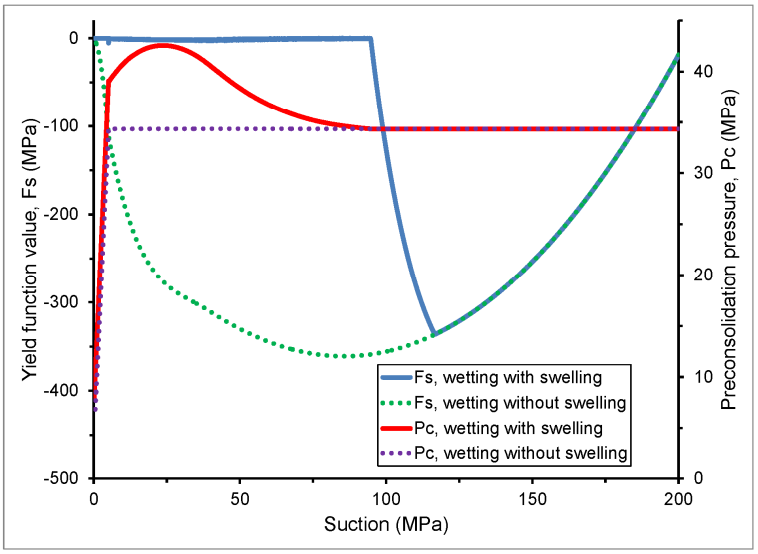

Fig. 26. Variation of the yield function value F_s and the preconsolidation pressure P_c based on numerically simulated oedometer free-swell testing of MX80 E-Mix granular bentonite, subjected to progressive wetting to saturation from an initial suction of 200 MPa

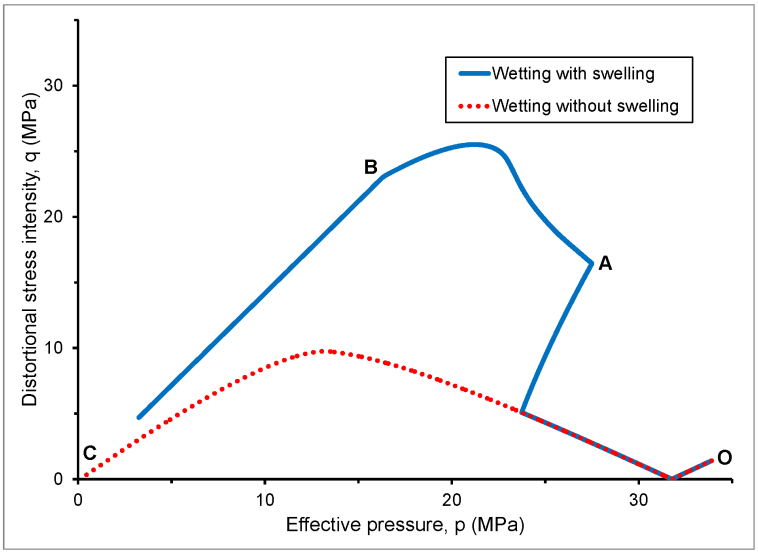

Fig. 27. Calculated p-q stress paths based on Eqs. (22) and (23) from the simulated free-swell testing of granular bentonite described in Fig. 31. Path OABC represents the general direction of the simulated tests

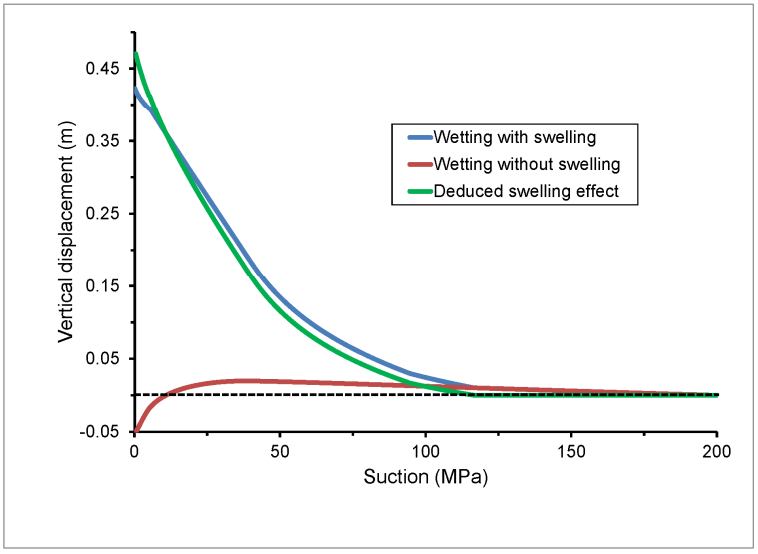

Fig. 28. Calculated axial displacement versus suction from the simulated free-swell testing of granular bentonite described in Fig. 31

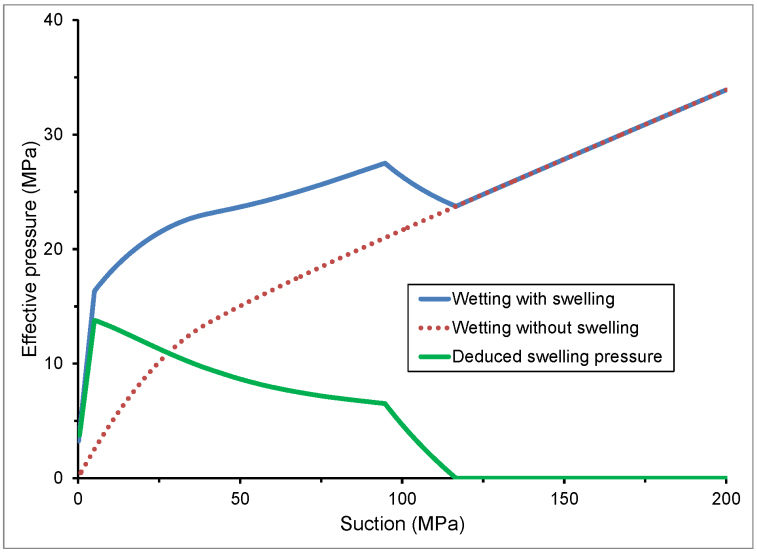

Fig. 29. Calculated effective pressure versus suction showing the effect of wetting on swelling pressure from the simulated free-swell testing of granular bentonite described in Fig. 31

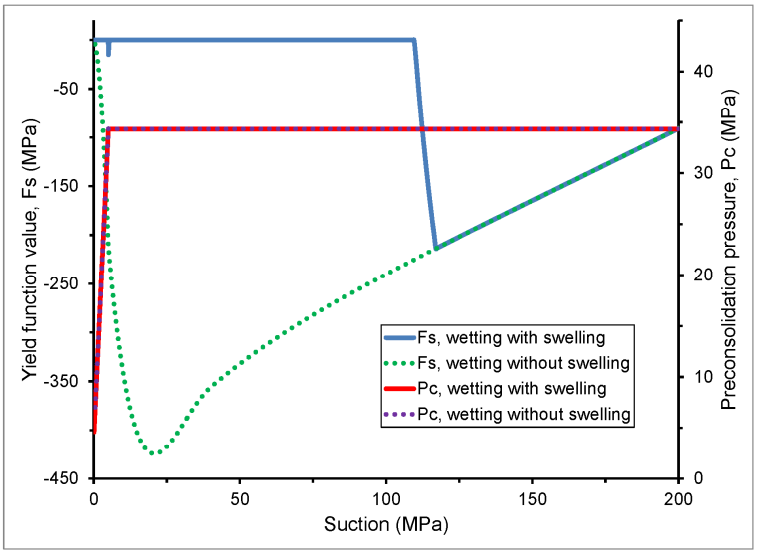

Fig. 30. Variation of the yield function value F_s and the preconsolidation pressure P_c based on numerically simulated oedometer confined (i.e., constant volume) swell testing of MX80 E-Mix granular bentonite, subjected to progressive wetting to saturation from an initial suction of 200 MPa

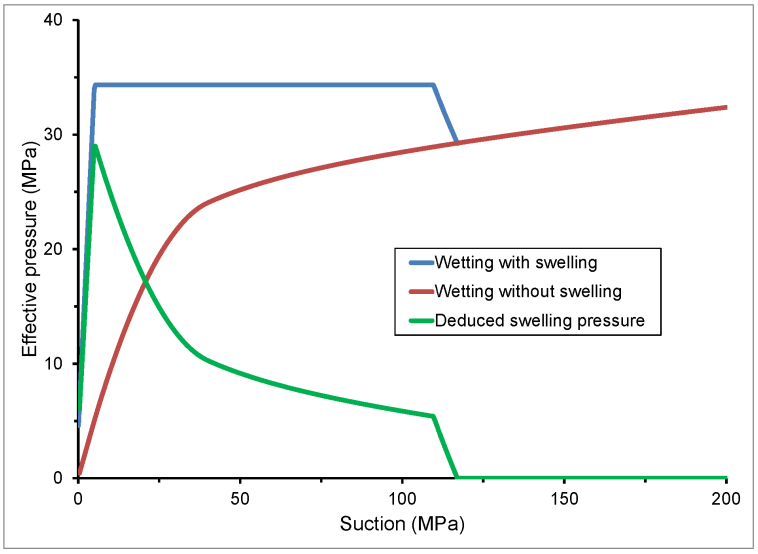

Fig. 31. Calculated effective pressure versus suction showing the effect of wetting on swelling pressure from the simulated constant-volume swell testing of granular bentonite described in Fig. 35

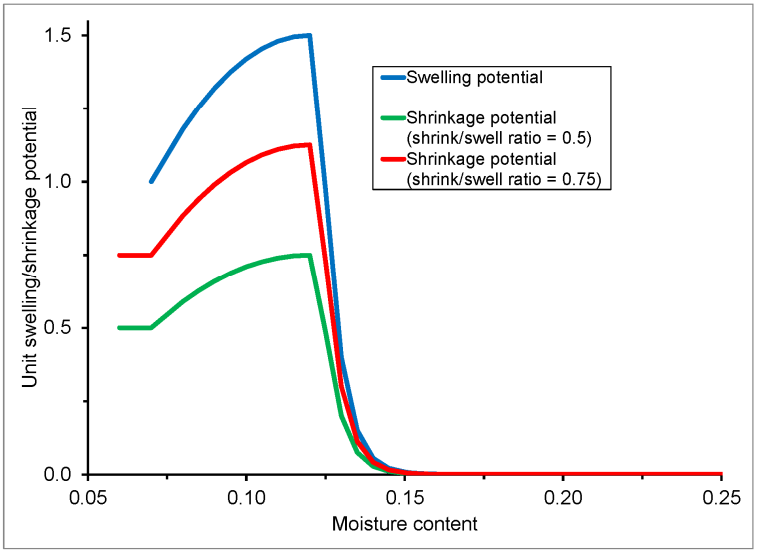

Fig. 32. Relationships between unit swelling/shrinkage potential (α_{CW}) and moisture content (θ_l) used in the numerical modeling example described in Section 3.4.

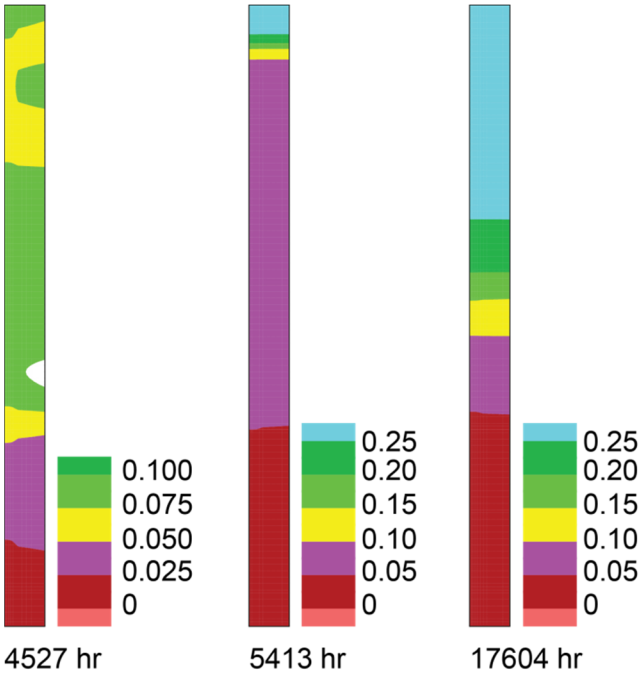

Fig. 33. Typical spatial distributions of moisture content (θ_l) used as input to the numerical modeling example described in Section 3.4.

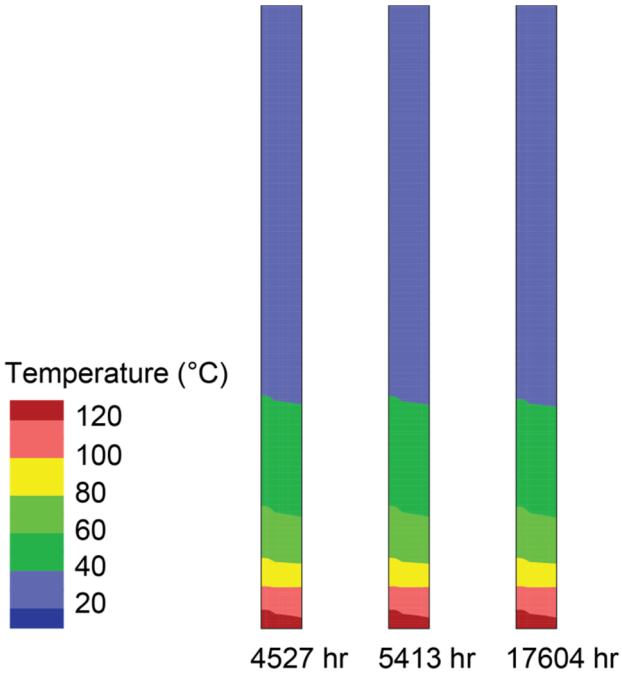

Fig. 34. Typical spatial distributions of temperature (T) used as input to the numerical modeling example described in Section 3.4.

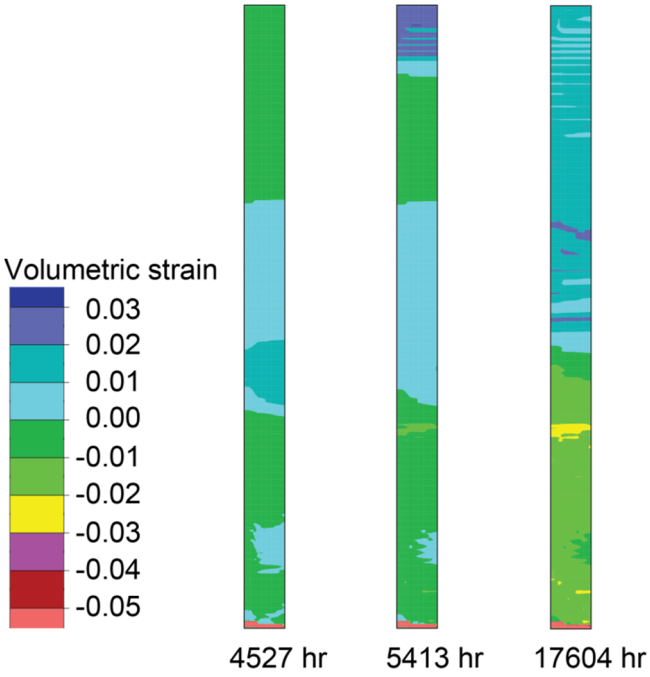

Fig. 35. Calculated spatial distributions of volumetric strain in the modeled bentonite column based on the numerical modeling example described in Section 3.4.

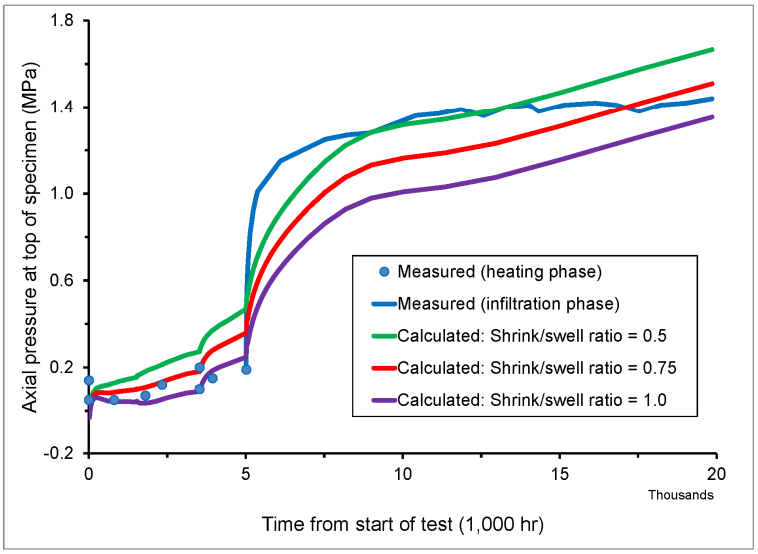

Fig. 36. Calculated histories of axial pressure at the top of the bentonite column compared with the measured axial pressure, based on the numerical modeling example described in Section 3.4.